

A panchromatic spatially resolved analysis of nearby galaxies - II. The main sequence - gas relation at sub-kpc scale in grand-design spirals

L. Morselli^{1,2*}, G. Rodighiero^{1,2}, A. Enia^{1,2}, E. Corbelli³, V. Casasola^{4,3},
L. Rodríguez-Muñoz¹, A. Renzini², S. Tacchella⁵, I. Baronchelli³, S. Bianchi³,
P. Cassata^{1,2}, A. Franceschini¹, C. Mancini^{1,2}, M. Negrello⁶, P. Popesso⁷, M. Romano^{1,2}

¹ *Dipartimento di Fisica e Astronomia, Università di Padova, vicolo dell'Osservatorio 3, I-35122 Padova, Italy*

² *INAF – Osservatorio Astrofisico di Padova, vicolo dell'Osservatorio 5, I-35122 Padova, Italy*

³ *INAF – Osservatorio Astrofisico di Arcetri, Largo E. Fermi 5, I-50125, Firenze, Italy*

⁴ *INAF – Istituto di Radioastronomia, Via P. Gobetti 101, I-40129, Bologna, Italy*

⁵ *Center for Astrophysics | Harvard & Smithsonian, 60 Garden St, Cambridge, MA 02138, USA*

⁶ *School of Physics and Astronomy, Cardiff University, The Parade, Cardiff CF24 3AA, UK*

⁷ *Excellence Cluster Universe, Boltzmann strasse 2, D-85748 Garching bei München, Germany*

Accepted 2020 June 18. Received YYY; in original form ZZZ

ABSTRACT

In this work we analyse the connection between gas availability and the position of a region with respect to the spatially resolved main sequence (MS) relation. Following the procedure presented in [Enia et al. \(2020\)](#), for a sample of five face-on, grand design spiral galaxies located on the MS we obtain estimates of stellar mass and star formation rate surface densities (Σ_{\star} and Σ_{SFR}) within cells of 500pc size. Thanks to HI 21cm and ¹²CO(2-1) maps of comparable resolution, within the same cells we estimate the surface densities of the atomic (Σ_{HI}) and molecular (Σ_{H_2}) gas and explore the correlations among all these quantities. Σ_{\star} , Σ_{SFR} and Σ_{H_2} define a 3D relation whose projections are the spatially resolved MS, the Kennicutt-Schmidt law and the molecular gas MS. We find that Σ_{H_2} steadily increases along the MS relation and is almost constant perpendicular to it. Σ_{HI} is nearly constant along the MS and increases in its upper envelope. As a result, Σ_{SFR} can be expressed as a function of Σ_{\star} and Σ_{HI} , following the relation $\log \Sigma_{\text{SFR}} = 0.97 \log \Sigma_{\star} + 1.99 \log \Sigma_{\text{HI}} - 11.11$. We show that the total gas fraction significantly increases towards the starburst regions, accompanied by a weak increase in star formation efficiency. Finally, we find that H₂/HI varies strongly with the distance from the MS, dropping dramatically in regions of intense star formation, where the UV radiation from newly formed stars dissociates the H₂ molecule, illustrating the self-regulating nature of the star formation process.

Key words: galaxies: evolution – galaxies: star formation – galaxies: spirals

1 INTRODUCTION

In the current model of galaxy formation and evolution stars form in dense clouds of molecular gas, thanks to the interplay of different physical mechanisms (magnetic fields, turbulence, shielding, feedback). Despite its complexity, this interplay translates in tight correlations between different physical quantities: *i*) between the surface density of the

star formation rate (Σ_{SFR}) and the surface density of the gas (Σ_{gas}), and *ii*) between the stellar mass surface density (Σ_{\star}) and Σ_{SFR} . The first relation, originally formulated by [Schmidt \(1959\)](#) using the gas volume density and the number of stars formed in the solar neighborhood, was subsequently derived by [Kennicutt \(1998\)](#) for radially averaged surface densities in external galaxies, and it is thus called the Kennicutt-Schmidt (KS) relation. The second, called main sequence (MS), was initially found using integrated quantities of star-forming galaxies (thus the total SFR and stellar

* E-mail: laura.morselli@unipd.it

mass M_{\star}) in Brinchmann et al. (2004) for local galaxies and later confirmed for high-redshift galaxies by several works (e.g. Salim et al. 2007; Noeske et al. 2007; Elbaz et al. 2007; Daddi et al. 2007). As both relations are intrinsically related to the process of star formation and thus to galaxy evolution as a whole, and because they are fundamental ingredients of theoretical models and simulations, they have been intensively studied in the past (e.g. Tan 2000; Boissier et al. 2003; Springel & Hernquist 2003; Krumholz & McKee 2005; Rodighiero et al. 2011; Krumholz et al. 2012; Whitaker et al. 2012; Kennicutt & Evans 2012; Kashino et al. 2013; Speagle et al. 2014; Hopkins et al. 2014; Genzel et al. 2015; Schreiber et al. 2015; Kurczynski et al. 2016; Santini et al. 2017; Tacchella et al. 2016; Orr et al. 2018; Pearson et al. 2018; Popesso et al. 2019; Morselli et al. 2019).

The KS law relates the fuel of star formation to its end product, stars; its shape has important effects on the depletion time of the gas ($t_{\text{depl}} = M_{\text{gas}}/\text{SFR}$, with M_{gas} the total gas mass), or equivalently on the efficiency of the star formation process ($\text{SFE} = t_{\text{depl}}^{-1} = \text{SFR}/M_{\text{gas}}$). In one of the earliest works, Kennicutt (1998) finds a super linear correlation (slope = 1.4-1.5) between the total gas and the SFR surface densities. Following this result, several papers investigate the relation between star formation and gas availability, considering different gas phases and star formation tracers, as well as exploring this link at different cosmic epochs (e.g. Wyder et al. 2009; Genzel et al. 2010; Tacconi et al. 2010; Genzel et al. 2012). Bigiel et al. (2008), Leroy et al. (2008, 2013) and Schrubba et al. (2011) exploit molecular and neutral gas observations of nearby galaxies to investigate how the relation between gas and star formation activity varies within galaxies and as a function of local and integrated properties. Overall, their findings indicate that the connection between star formation and molecular gas is a linear relation (i.e., slope ~ 1), thus implying a constant molecular SFE and t_{depl} (around 2.2 Gyr). Leroy et al. (2013) find second order variations in the molecular gas t_{depl} and study how some of them can be related to variations in the α_{CO} conversion factor between CO luminosity and H_2 mass, while further variability might arise as a consequence of galaxy properties. Bigiel et al. (2010), instead, study the relation between recent SF activity and HI outside the optical disc, in regions where HI represents the totality of the ISM, and find significant spatial correlation between FUV (tracing recent dust-unobscured star formation) and HI density. They also find that the SFE (t_{depl}) decreases (increases) with increasing radius. Similarly, Roychowdhury et al. (2015) study the spatially resolved KS relation on sub-kpc and kpc scales in the HI dominated regions of nearby spirals and irregular galaxies and find that gas consumption time-scales are longer compared to H_2 dominated regions (lower SFE). Other works investigated, at earlier cosmic epoch, the spatially resolved (e.g. Genzel et al. 2013; Freundlich et al. 2013) and integrated (Freundlich et al. 2019, e.g.) KS relation. In particular, Freundlich et al. (2019) obtain a linear galaxy-averaged molecular KS relation, implying that galaxies at different cosmic epochs have similar star formation timescales. This is consistent with the results of Peng & Renzini (2020), that find that the sSFR (SFR/M_{\star}) and M_{H_2}/M_{\star} have the same redshift evolution, thus implying a linear KS law. On the other hand, galaxy-to-galaxy variations in the molecular gas - star formation relation have also been reported. For exam-

ple, Ford et al. (2013) and Shetty et al. (2013, 2014b,a) find evidence for a sub-linear relation within galaxies and for the combined samples. Also Casasola et al. (2015) find galaxy-to-galaxy variations of the spatially resolved KS relation, and underline that the slope can be both sub-linear and super-linear, depending on the spatial scale. de los Reyes & Kennicutt (2019) revisit the integrated KS law in local, normal star-forming galaxies and find that spirals lie on a tight log-linear relation with slope 1.41 ± 0.07 (when considering both the neutral and molecular gas) while dwarfs populate the region below it.

The second fundamental relation, the MS, relates stars that have already formed to the ongoing SFR. The existence of the MS up to $z \sim 4$ (characterised by a non-evolving slope and scatter and an increasing normalisation with increasing redshift, e.g. Speagle et al. 2014; Popesso et al. 2019) was interpreted in the framework of gas-regulated galaxy evolution, according to which galaxies grow along the MS thanks to the continuous replenishment of their gas supply (e.g. Dekel et al. 2009; Bouché et al. 2010; Lilly et al. 2013). The observation of outliers located above the MS relation (starburst are generally classified in literature as galaxies having a SFR that is a factor 4 higher than the MS value at fixed stellar mass, e.g. Rodighiero et al. 2011) at different cosmic epochs sparked the interest on whether these sources: *i*) have larger gas reservoirs (thus a higher gas fraction, $f_{\text{gas}} = M_{\text{gas}}/(M_{\text{gas}} + M_{\star})$, e.g. Lee et al. 2017), *ii*) are more efficient in converting gas into stars (thus a higher SFE, e.g. Solomon et al. 1997; Daddi et al. 2010; Silverman et al. 2015, 2018; Ellison et al. 2020a), or *iii*) a combination of both (e.g. Saintonge et al. 2011a, 2012; Huang & Kauffmann 2014; Scoville et al. 2017; Tacconi et al. 2018). In the recent years, the advent of large integral field spectroscopic (IFS) surveys revealed that the integrated MS relation originates at smaller scales (up to the sizes of molecular clouds), thus implying that the star formation process is regulated by physical processes that act on sub-galactic scales (Cano-Díaz et al. 2016; Hsieh et al. 2017; Lin et al. 2017; Abdurro'uf & Akiyama 2017; Medling et al. 2018; Hall et al. 2018; Cano-Díaz et al. 2019; Vulcani et al. 2019; Bluck et al. 2020; Enia et al. 2020). Despite a general consensus on the existence of the spatially resolved MS, the slope, intercept and scatter of the relation vary significantly among different works, depending on the sample selection, SFR indicator, dust correction, and fitting procedure. Moreover, some authors find that the spatially resolved relation vary dramatically from galaxy to galaxy. Recently, the combination of MaNGA (Mapping Nearby Galaxies at APO, Bundy et al. 2015) and ALMaQUEST (the ALMA-MaNGA QUEnching and STar formation survey) allowed the study of the link between the spatially resolved MS and gas reservoirs and the investigation of the nature of starburst regions within galaxies. By analysing 14 MS galaxies, Lin et al. (2019) suggest that the MS relation originates from two more fundamental relations: the molecular KS and the so-called *molecular gas main sequence* (MGMS), a relation between Σ_{\star} and Σ_{H_2} . Ellison et al. (2020b) exploit 34 galaxies in ALMaQUEST to study the nature of variations in the SFR on kpc scales. They find that while the average SFR is regulated by the availability of molecular gas, the scatter of the spatially resolved MS (and thus variations with respect to the average SFR value) originates in variations of the SFE. Dey et al. (2019), using optical IFU and CO ob-

Table 1. Properties of the galaxies in our sample: (1) galaxy name; (2,3) RA and Dec coordinates in J2000; (4) total M_{\star} from SED fitting; (5) total SFR computed from Eq. 1 with L_{UV} and L_{IR} from SED fitting; (6,7) distance in Mpc and radius in kpc at which the optical surface brightness falls below 25 mag arcsec⁻², both taken from the HyperLEDA data base; (8) total HI mass in R_{25} ; (9) total H_2 mass in R_{25} ; (10) morphological T type, taken from HyperLEDA; (11) central metallicity computed using the O3N2 index, and taken from the DustPedia archive.

| Galaxy Name | RA [deg] | DEC [deg] | $\log M_{\star}$ [M_{\odot}] | SFR [M_{\odot}/yr] | D [Mpc] | R_{25} [kpc] | $\log M_{\text{HI}}$ [M_{\odot}] | $\log M_{\text{H}_2}$ [M_{\odot}] | T | $12 + \log(\text{O}/\text{H})$ |
|----------------|-------------|--------------|-------------------------------------|----------------------------------|------------|-------------------|---|--|-----|---|
| NGC0628 (M74) | 24.174 | 15.7833 | 10.31±0.15 | 1.78±0.41 | 10.14 | 14.74 | 9.54±0.18 | 9.39±0.20 | 5.2 | 8.693±0.001 |
| NGC3184 | 154.5708 | 41.4244 | 10.13±0.10 | 1.02±0.10 | 11.64 | 12.55 | 9.38±0.14 | 9.20±0.24 | 5.9 | 8.766 ^{+0.014} _{-0.013} |
| NGC5194 (M51a) | 202.8025 | 47.1952 | 10.74±0.20 | 3.68±0.26 | 8.59 | 17.23 | 9.43±0.17 | 9.86±0.22 | 4.0 | 8.824 ^{+0.017} _{-0.016} |
| NGC5457 (M101) | 210.8025 | 54.3491 | 10.37±0.13 | 3.00±0.15 | 7.11 | 24.81 | 10.15±0.14 | 9.41±0.18 | 5.9 | 8.528 ^{+0.006} _{-0.007} |
| NGC6946 | 308.71905 | 60.15361 | 10.61±0.13 | 3.51±0.15 | 6.73 | 24.81 | 9.41±0.15 | 9.74±0.17 | 5.9 | 8.746 ^{+0.067} _{-0.070} |

servations collected in the EDGE-CALIFA survey (CARMA Extragalactic Database for Galaxy Evolution Bolatto et al. 2017, see also Barrera-Ballesteros et al. 2020), find that Σ_{SFR} is a function of both Σ_{\star} and Σ_{H_2} but, differently from Lin et al. (2019), the relation with the stellar mass is statistically more significant than the one with the molecular gas. Early works on the formation of molecular hydrogen in the ISM, such as Elmegreen (1993) and Blitz & Rosolowsky (2006), have underlined the role of the disc hydrostatic pressure, and hence of Σ_{\star} , in promoting the formation of molecules. Also the works of Shi et al. (2011) and Shi et al. (2018), that propose an *extended KS law* expressed as a proportionality between Σ_{SFE} and Σ_{\star} , emphasise the role of existing stars in setting the current production of stars, which indeed is the very nature of the MS.

In this paper, we build on the work presented in Enia et al. (2020, hereafter Paper I) and analyse the sub-kpc relation between the surface densities of star formation, gas in different phases, and stellar mass in 5 local grand-design spirals. In Paper I we exploit multiwavelength observations in more than 20 photometric bands to obtain spatially resolved estimates of Σ_{\star} and Σ_{SFR} on different physical scales, from few hundred parsecs to 1.5 kpc, via SED fitting. We use these estimates to study the spatially resolved MS relation and find the slope to be consistent for different spatial scales, as well as with the slope of the integrated relation. Here, we aim at analysing under which gas properties different spatial regions populate different loci of the spatially resolved MS, thus trying to understand whether the SFR is more connected to the gravity of the disc (dominated by stars up to $\sim 2/3$ of the optical radius) or with the availability of fuel, or a combination of both. We exploit observations in more than 20 photometric bands to derive accurate SFR and M_{\star} maps to compare to HI and H_2 maps. We discuss the origin of the spatially resolved MS, in terms of its slope and scatter.

The structure of the paper is the following: in Section 2 we give a short description of the data used in this work; in Section 3 we present our results at 500 pc resolution; in Section 4 we analyse the implications of our results on the existence of the MS relation and on how SFE and f_{gas} vary with varying SFR. Finally, in Section 5 we summarise our findings. The assumed IMF is Chabrier (2003), cosmology is Λ CDM with parameters from Planck Collaboration et al. (2016).

2 DATA

This work is based on multiwavelength observations of five nearby face-on spiral galaxies: NGC0628, NGC3184, NGC5194, NGC5457, and NGC6946. Four out of five galaxies are in common with Paper I: they are the ones observed in 23 photometric bands, and included in the THINGS and HERACLES surveys. NGC6946 was initially excluded from the Paper I sample since it lacked optical observations (the five Sloan optical filters). We tested for the sample in Paper I how the SED fitting routine results change excluding these five photometric points, finding that they are nearly unchanged. Following this, we are including NGC6946 in this analysis. The observations in 23 different bands (18 for NGC6946) have been collected in the DustPedia¹ (Davies et al. 2017; Clark et al. 2018) archive; more details on the data set can be found in Paper I and references therein. The main properties of the galaxies in this sample are shown in Table 1. We highlight two properties of our sample: *i*) according to the integrated SFR and M_{\star} values, the objects in our sample are MS galaxies, located within 0.2 dex from the relation obtained in Paper I, and *ii*) three out of five sources are classified as SAB spirals (NGC3184, NGC5457 and NGC6946), thus show evidence of a bar component.

2.1 SFRs, stellar mass, and distance from the MS

The spatially resolved measurements at 500 pc resolution of Σ_{\star} , Σ_{SFR} and distance from the MS (Δ_{MS}), have been obtained following the procedure presented in Paper I. Briefly, we select 8 nearby, face-on, grand design spiral MS galaxies with $\log M_{\star} \sim 10.4\text{--}10.6 M_{\odot}$, and perform spatially resolved SED fitting to 23 photometric bands using MAGPHYS (da Cunha et al. 2008). In particular, we performed SED fitting on cells having two different side measurements: 8 arcsec (thus a varying physical scale between 290pc and 700pc, depending on the distance of the galaxies) and 1.5 kpc. Here we implement an improved procedure, and performed SED fitting at a common resolution of 500 pc (as discussed in Paper I, these scales are higher than the ones where the energy-balance criterion holds, $\sim 200\text{--}400$ pc). The procedural improvements are the following: *i*) we estimate the noise on the photometry of each cell from the rms maps (while in Paper I

¹ The DustPedia data base is available at <http://DustPedia.astro.noa.gr>

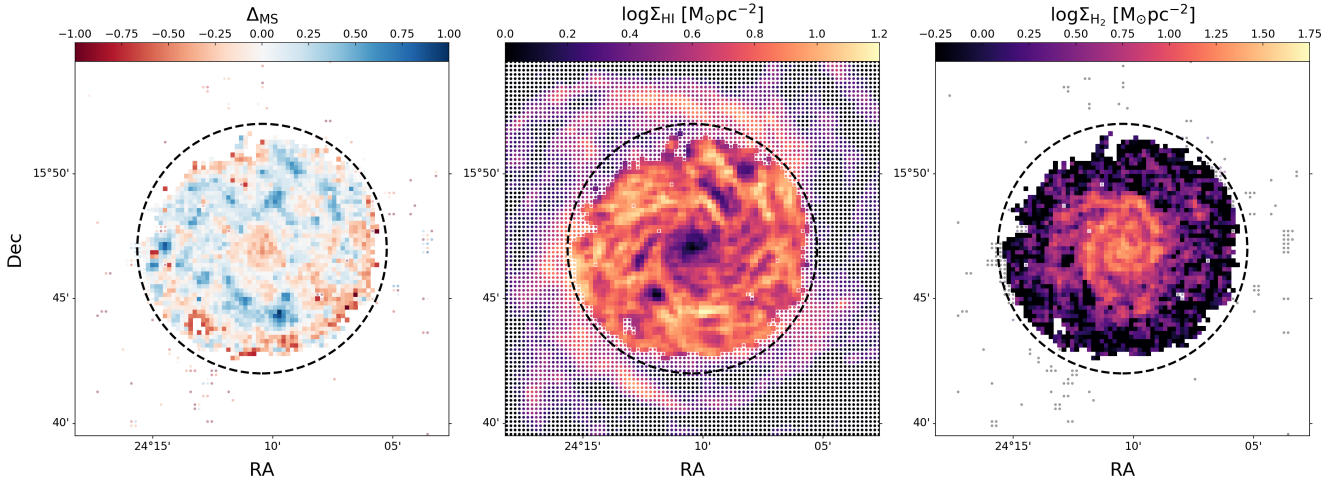


Figure 1. Spatially resolved properties of NGC0628: Δ_{MS} (left panel), $\log \Sigma_{\text{HI}}$ (central panel), and $\log \Sigma_{\text{H}_2}$ (right panel). The dashed circle marks the optical radius of the galaxy.

we used the DustPedia photometry signal-to-noise ratio); *ii*) if a cell has more than 10 bands with $\text{SNR} < 2$ it is automatically excluded from the SED fitting procedure, thus reducing computational time. These improvements influence the χ^2 estimation in MAGPHYS, increasing the number of accepted points within the optical radius, and leading to cleaner results in the outer part of galaxies, where the photometry is fainter. The slope and intercept of the spatially resolved MS given in Paper I do not change when these improvements are implemented in the pipeline.

In each cell, the SFR is computed as the sum of unobscured (SFR_{UV}) and obscured (SFR_{IR}) star formation activity, obtained using the relations of [Bell & Kennicutt \(2001\)](#) and [Kennicutt \(1998\)](#) (reported to Chabrier IMF):

$$\text{SFR} = 0.88 \cdot 10^{-28} L_{\text{UV}} + 2.64 \cdot 10^{-44} L_{\text{IR}}, \quad (1)$$

where L_{UV} and L_{IR} are taken from the best fitting SED and are the luminosity (in $\text{erg s}^{-1} \text{ Hz}^{-1}$) at 150nm and the one (in erg s^{-1}) integrated between 8 and $1000 \mu\text{m}$, respectively. As shown in Fig. 3 of Paper I, the SFR computed following Eq. 1 and the one that MAGPHYS gives as output, are highly consistent. Here, for consistency with Paper I, we use the SFRs estimated with Eq. 1, but the results would not change when considering the SFRs given as output of the SED fitting procedure.

As the sample of galaxies used here differs from the one of Paper I, we decided to recompute the spatially resolved MS for this sample, but following the same procedure, i.e., 1) by fitting with a log-linear relation the median values of $\log \Sigma_{\text{SFR}}$ in bins of $\log \Sigma_{\star}$, using EMCEE ([Foreman-Mackey et al. 2013](#)) and considering 10 bins in the $\log \Sigma_{\star}$ range $[6.5:8.5] \text{ M}_{\odot} \text{pc}^{-2}$, plus an additional bin to include the few points between $[8.5:9.5] \text{ M}_{\odot} \text{pc}^{-2}$, and 2) by implementing an orthogonal distance regression (ODR) technique. The slope and intercept of the MS are $0.76(\pm 0.20)$ and $-8.15(\pm 1.63)$ with the first method, and $0.87(\pm 0.01)$ and $-8.94(\pm 0.06)$ with the second. These estimates are consistent with the ones in Paper I. In the following analysis we make use of the distance from the MS relation computed with the binning technique, but our results do not change when considering the ODR MS relation.

For each region we compute the distance from the MS as the difference between $\log \Sigma_{\text{SFR}}$ and the MS value (in log) estimated for the Σ_{\star} of the region, thus: $\Delta_{\text{MS}} = \log \Sigma_{\text{SFR}} - (0.76 \log \Sigma_{\star} - 8.15)$. The left panel of Fig. 1 shows, as an example, the Δ_{MS} map of NGC0628; cells in red are located below the spatially resolved MS, while the ones in blue are located above the relation (the Δ_{MS} maps of the other galaxies in the sample are shown in Appendix B). Within the optical radius (the dashed circle) we are able to recover most of the cells, especially at $r < 0.9 R_{25}$ ². We emphasise here that the MS relation we obtain is well defined also in the outer parts of the optical disc, where the SFR and M_{\star} are small in absolute values. We refer the reader to Paper I for details on the SED fitting procedure, as well as for how the spatially resolved MS relation is obtained.

2.2 Neutral gas: HI 21cm observations

Neutral hydrogen mass surface densities (Σ_{HI}) are measured from 21cm maps available from the THINGS survey (The HI Nearby Galaxy Survey, [Walter et al. 2008](#)). These observations have been carried out with the Very Large Array (VLA) and are characterized by a high angular resolution (6 arcsec and 10 arcsec in the robust and natural weighting, respectively). To compute the HI surface brightness, Σ_{HI} , we first convolve the 21cm natural-weighted intensity maps, given in $\text{Jy beam}^{-1} \text{ m s}^{-1}$, to the resolution of the worst of the 23 photometric bands used in the SED fitting (the one of SPIRE350, 24 arcsec, see Paper I) using a Gaussian kernel. We used the beam sizes given in Table 2 of [Walter et al. \(2008\)](#) and Eq. 1 to obtain the flux in K km s^{-1} and then estimate Σ_{HI} from Eq. 5 of [Walter et al. \(2008\)](#) (that does not include a correction for helium). We compute the sensitivity limit from our maps of Σ_{HI} at 500 pc resolution and find $\Sigma_{\text{HI,lim}} \sim 2 \text{ M}_{\odot} \text{pc}^{-2}$. The central panel of Fig. 1 shows the distribution of Σ_{HI} in NGC0628. As in several other spiral

² R_{25} is defined as the length of the projected semi-major axis of a galaxy at the isophotal level 25 mag/arcsec² in the B-band and it is taken from the HyperLEDA data base ([Makarov et al. 2014](#)).

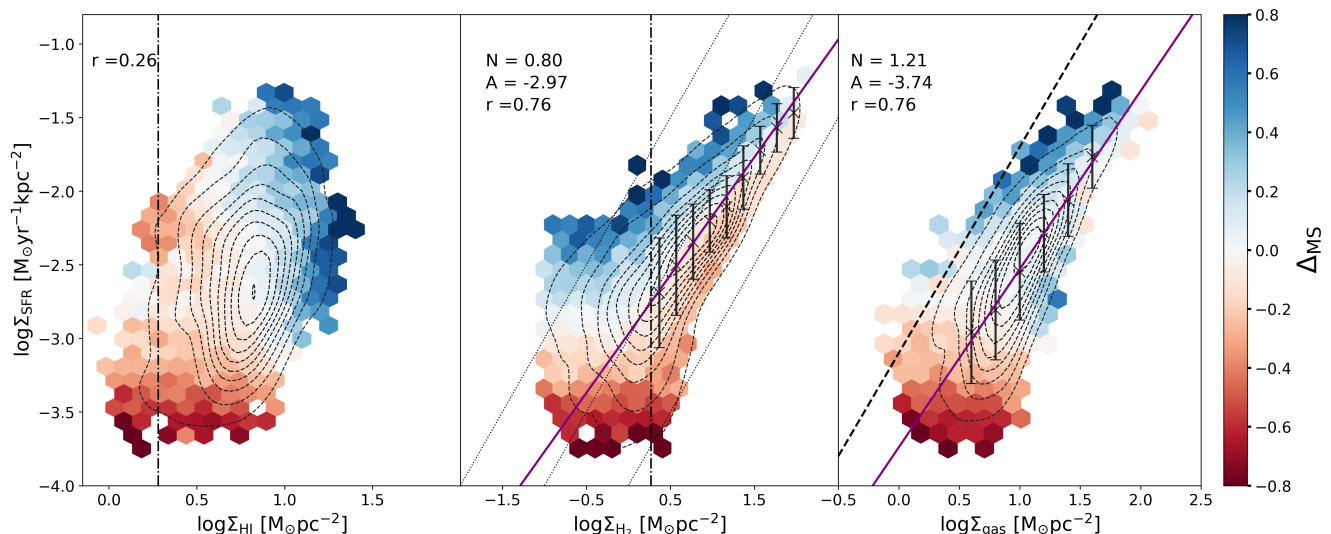


Figure 2. Relations between Σ_{SFR} and Σ_{HI} (left panel), Σ_{H_2} (middle panel) and Σ_{gas} (for the total HI+H₂ gas, right panel) colour coded as a function of the median value of Δ_{MS} in each bin. Only bins containing a minimum number of 3 cells are shown in the plot. The dashed contours encircle the areas of the plane containing from 10% to 90% of the data, at steps of 10%. The sensitivity limits are represented by the dotted-dashed black lines. The purple solid lines in the middle and right panel represent the best fit to the data obtained fitting the points marked with crosses; the corresponding slope (N) and intercept (A) are written in the panels, together with the Spearman correlation coefficient r . In the central panel, the dotted lines mark constant molecular t_{depl} of 10^8 , 10^9 , and 10^{10} yr from top to bottom. In the right panel, the dashed black line is the fit to local ULIRGs and SMGs taken from [Daddi et al. \(2010\)](#).

galaxies, the HI is centrally depressed (e.g. [Casasola et al. 2017](#)), and it extends on radius that are significantly larger than the optical radius ([Swaters et al. 2002](#); [Wang et al. 2013](#)). The values of M_{HI} within R_{25} are reported in Table 1. For the galaxies in our sample, the HI gas-to-stellar mass ratio (M_{HI}/M_{\star}) within R_{25} varies from 5% to 60%.

2.3 Molecular gas: CO observations

The molecular gas surface density, Σ_{H_2} , is computed using the $^{12}\text{CO}(2-1)$ intensity maps from the HERACLES survey (The HERA CO-Line Extragalactic Survey, [Leroy et al. 2009](#)). These observations were made with the IRAM 30m telescope and have an angular resolution of 11 arcsec. As for Σ_{HI} we convolve the images using a Gaussian kernel to the resolution of SPIRE350. We estimated Σ_{H_2} using Eq. 4 of [Leroy et al. \(2009\)](#), considering a metallicity independent conversion factor X_{CO} ($X_{\text{CO}} = N(\text{H}_2)/I_{\text{CO}}$, where $N(\text{H}_2)$ is the H₂ column density and I_{CO} is the line intensity) equal to $2 \cdot 10^{20} \text{ cm}^{-2} (\text{K km s}^{-1})^{-1}$ (the typical value for disc galaxies, see e.g. [Bolatto et al. 2013](#)), and a CO line ratio $I_{\text{CO}(2-1)}/I_{\text{CO}(1-0)} = 0.8$ (e.g. [Leroy et al. 2009](#); [Schruba et al. 2011](#); [Casasola et al. 2015](#)). We divide by a factor 1.36 that is included in Eq. 4 of [Leroy et al. \(2009\)](#) to remove the helium contribution. In Sec. 3 we show that the results presented here remain true when considering a metallicity-dependent X_{CO} factor, using the $X_{\text{CO}}-(12+\log \text{O}/\text{H})$ relation of [Genzel et al. \(2011\)](#) and the spatially resolved metallicity measurements collected in DustPedia. The sensitivity limit, computed as the rms of our $\log \Sigma_{\text{H}_2}$ maps at 500pc resolution, is $\log \Sigma_{\text{H}_2, \text{lim}} = 0.4 M_{\odot} \text{ pc}^{-2}$. For the regions corresponding to a negative flux of $^{12}\text{CO}(2-1)$, in the $\Sigma_{\text{H}_2, \text{lim}}$ map we replace the value with a randomly generated number between 0 and the sensitivity limit, so that Σ_{H_2} can be computed as

an upper limit. While this step does not influence our results concerning H₂, it allows us to extend the analysis also to the regions where H₂ is not detected. The right panel of Fig. 1 shows the distribution of Σ_{H_2} in NGC0628. The H₂ is centrally concentrated, and mostly below the sensitivity limit for $r > 0.5 R_{25}$. For the galaxies in our sample, the H₂ gas-to-stellar mass ratio (M_{H_2}/M_{\star}) within R_{25} is almost constant around 11-14%.

3 RESULTS

Before analysing the spatially resolved connection between star formation and gas components, we briefly comment on the integrated properties of the galaxies in our sample. It is worth underlying that, within R_{25} , three out of five galaxies have similar amount of neutral and molecular gas (M_{H_2} and M_{HI}), within the uncertainties. This is consistent with the results of [Casasola et al. \(2020\)](#), as they find that, within R_{25} , galaxies with morphological type $T = 4, 5, 6$ have $M_{\text{H}_2}/M_{\text{HI}} = 0.91, 1$ and 1.05 respectively. For NGC5457 and NGC5194 the average value associated to their morphological type does not describe well their gas properties. It is well known that NGC5457 is likely to have experienced a recent event of gas accretion ([Mihos et al. 2013](#); [Vílchez et al. 2019](#)) which can explain the HI rich outer disc and its high total HI mass. A high molecular gas mass fraction, as for NGC5194, is likely the result of tidal stirring by a companion.

3.1 Dependency of the SFR on gas

With the data set in our hands, we first investigate the spatially resolved relations between the SFR and the different gas phases, by analysing how Σ_{SFR} relates to Σ_{HI} , Σ_{H_2} , and

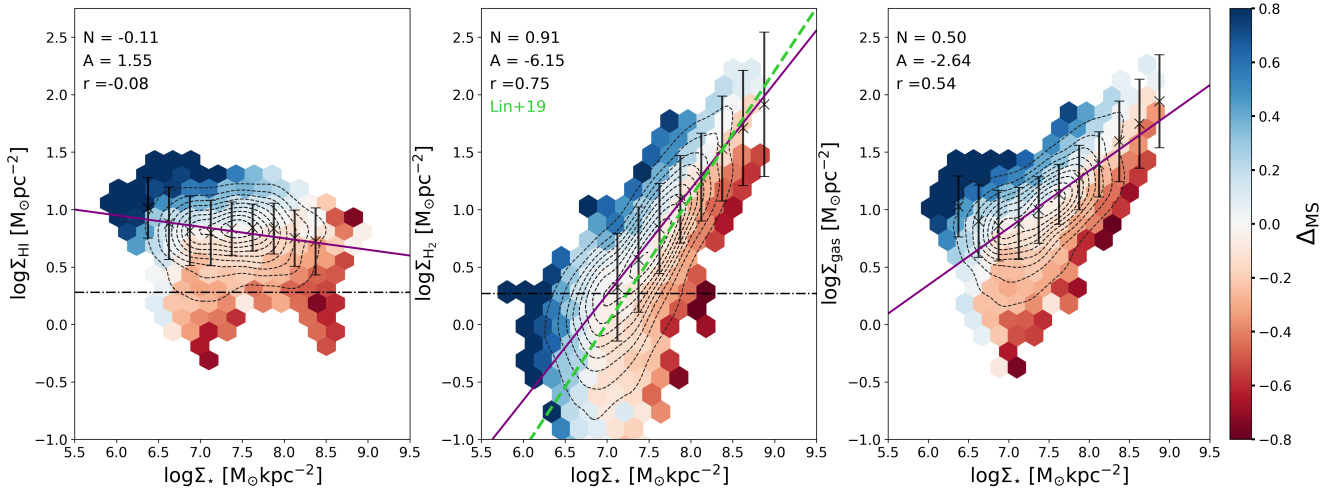


Figure 3. Distributions of the regions in the $\log \Sigma_{\star}$ - $\log \Sigma_{\text{HI}}$ plane (left panel), $\log \Sigma_{\star}$ - $\log \Sigma_{\text{H}_2}$ plane (central panel) and $\log \Sigma_{\star}$ - $\log \Sigma_{\text{gas}}$ plane (right panel). Each hexagonal bin the plane has been colour coded according to the average value of Δ_{MS} , as in Fig. 2. The purple solid lines are the best fit relations obtained by fitting the average values of $\log \Sigma_{\text{HI}, \text{H}_2, \text{gas}}$ in bins of $\log \Sigma_{\star}$, as marked with black crosses; the slope (N) and intercept (A) of the best fit are written in the panels, together with the Spearman correlation coefficient r . The green dashed line in the central panel is the MGMS of [Lin et al. \(2019\)](#), re-scaled to a Chabrier IMF.

Σ_{gas} . This last quantity is computed as the sum of the neutral and molecular component for all the regions where the Σ_{H_2} is above the sensitivity limit, while it is equal to Σ_{HI} otherwise, and it is thus a lower limit. The results of this exercise are shown in Fig. 2.

As expected, no significant correlation is found between Σ_{SFR} and Σ_{HI} (Spearman correlation coefficient $r = 0.26$), while tight correlations are present between Σ_{SFR} and Σ_{H_2} , and Σ_{SFR} and Σ_{gas} ($r = 0.76$), confirming several results in the literature (e.g. [Bigiel et al. 2008](#); [Kumari et al. 2020](#)). In Fig. 2 we add the information on how regions located at different distance from the spatially resolved MS populate the $\log \Sigma_{\text{SFR}} - \log \Sigma_{\text{HI}/\text{H}_2/\text{gas}}$ plane. To do so, we divide the $\log \Sigma_{\text{SFR}} - \log \Sigma_{\text{HI}/\text{H}_2/\text{gas}}$ planes in bins colour coded according to the median value of Δ_{MS} in each bin. We observe that regions above the MS are found in correspondence to the highest Σ_{HI} , but span a wide range of Σ_{H_2} values. Analogously, regions located below the MS are preferentially found at lower Σ_{HI} , while are characterized by Σ_{H_2} spanning the whole range of possible values. For $\log \Sigma_{\text{SFR}} > -2$ the trend between $\log \Sigma_{\text{HI}}$ and Δ_{MS} is less evident; this is due to the fact that we are not well sampling the region below the MS, as shown in Fig. 5 of Paper I, and confirmed by the decrease of the scatter of the spatially resolved MS at the higher stellar surface densities. Analogously, the points with $\log \Sigma_{\text{SFR}} < -3$ are mostly found on the MS or below it, thus hiding a possible trend at the lowest SFRs. When considering the total gas, we see that regions closer to the relation that describes local Ultra-Luminous IR Galaxies (ULIRGs) and sub-mm galaxies (dashed black lines, taken from [Daddi et al. 2010](#)) are the ones located above the relation. On the other hand, the general behaviour between the distance from the best fit relation and the distance from the MS is less regular than in the case of molecular gas. Indeed, the central panel of Fig. 2 suggests that the spatially resolved MS is intrinsically linked to the molecular gas - SFR relation, as MS regions (in white) fall very consistently along the $\log \Sigma_{\text{SFR}} - \log \Sigma_{\text{H}_2}$

relation. Regions that populate the upper (lower) envelope of the molecular KS law are also found in the upper (lower) envelope of the spatially resolved MS relation. This is qualitatively consistent with what found by [Ellison et al. \(2020b\)](#) when analysing the molecular gas - SFR relation exploiting ALMA and MaNGA data, on kpc scales.

By fitting the average values of $\log \Sigma_{\text{SFR}}$ in bins of $\log \Sigma_{\text{H}_2}$ and $\log \Sigma_{\text{gas}}$ (both above the sensitivity limit of $\log \Sigma_{\text{H}_2}$) we find the following scaling relations (slopes N and intercepts A are also written in the corresponding panels):

$$\log \Sigma_{\text{SFR}} = 0.80(\pm 0.12) \cdot \log \Sigma_{\text{H}_2} - 2.97(\pm 0.85) \quad (2)$$

and

$$\log \Sigma_{\text{SFR}} = 1.21(\pm 0.18) \cdot \log \Sigma_{\text{gas}} - 3.74(\pm 1.15) \quad (3)$$

The two correlations have equal strength according to the Spearman coefficient, and their scatter is in both cases smaller than the one of the spatially resolved MS: 0.19 for the $\log \Sigma_{\text{H}_2} - \log \Sigma_{\text{SFR}}$ relation and 0.17 for the $\log \Sigma_{\text{gas}} - \log \Sigma_{\text{SFR}}$. The relation between $\log \Sigma_{\text{SFR}}$ and $\log \Sigma_{\text{H}_2}$ is sub-linear, but becomes linear when the ODR fitting is applied. We retrieve a molecular t_{depl} that varies between 1.6 and 3 Gyr. These results are in agreement with the typical t_{depl} in normal spiral galaxies (see, e.g. [Bigiel et al. 2008](#); [Saintonge et al. 2011b](#); [Leroy et al. 2013](#); [Casasola et al. 2015](#)). It is worth noticing that the slope of the spatially resolved KS relation obtained from the molecular and total gas are consistent, within errors, with the integrated relations (e.g. [Genzel et al. 2010](#); [Kennicutt & Evans 2012](#); [Tacconi et al. 2013](#); [de los Reyes & Kennicutt 2019](#); [Freundlich et al. 2019](#)), similar to what is found when comparing the spatially resolved and integrated MS relation. The scatter of the integrated relation is instead significantly higher (e.g. 0.28 in [de los Reyes & Kennicutt 2019](#)).

Finally, we underline here that the trends observed in Fig. 2 are not driven by one or few of the galaxies in our sample, but by and large are common to all five galaxies in

our sample. Slope and intercept of the $\log \Sigma_{\text{H}_2}$ - $\log \Sigma_{\text{SFR}}$ and $\log \Sigma_{\text{gas}}$ - $\log \Sigma_{\text{SFR}}$ relations are summarised in Table 2.

3.2 Dependency of gas distribution on stellar mass

As the trends shown in Fig. 2 with Δ_{MS} are related to variations of the gas content with M_{\star} , we show in Fig. 3 how the surface densities of neutral, molecular and total gas vary as a function of Σ_{\star} . The left panel of Fig. 3 shows that a very weak anti-correlation is found between $\log \Sigma_{\star}$ and $\log \Sigma_{\text{HI}}$. Indeed, when fitting the average values of $\log \Sigma_{\text{HI}}$ in bins of $\log \Sigma_{\star}$, the slope of the correlation is -0.11 ± 0.07 . We stress that every galaxy shows a trend of decreasing Σ_{HI} towards the central regions, as in the central region the high pressure favours the HI to H₂ transition and most of the gas is in molecular form, but such a decrease can be more or less pronounced from galaxy to galaxy, and does not follow a universal behaviour. Starbursting regions are preferentially located at $r > 0.5 R_{25}$, where the surface density of stars falls below $10^7 M_{\odot} \text{pc}^{-2}$, and are generally found along the spiral arms.

The relation between $\log \Sigma_{\star}$ and $\log \Sigma_{\text{H}_2}$, shown in the central panel of Fig. 3 is consistently common to all five galaxies and gives birth to a very tight correlation, the MGMS (Lin et al. 2019). The MGMS (re-scaled to a Chabrier IMF) of Lin et al. (2019) is indicated with a green dashed line in the central panel of Fig. 3 and has a slope of 1.1. To obtain the slope of our MGMS relation, we fit the average values of $\log \Sigma_{\text{H}_2}$ in bins of $\log \Sigma_{\star}$, restricting the analysis to stellar surface densities where the average value of $\log \Sigma_{\text{H}_2}$ is above the sensitivity limit. We find:

$$\log \Sigma_{\text{H}_2} = 0.91(\pm 0.29) \cdot \log \Sigma_{\star} - 6.15(\pm 2.11) \quad (4)$$

This relation has a scatter of 0.22 dex, similar to that obtained for the MS (0.23dex) and the Spearman coefficient is the same as for the $\log \Sigma_{\text{H}_2/\text{gas}}$ - $\log \Sigma_{\text{SFR}}$ relations. We find a slope that is consistent within the error with the one of Lin et al. (2019), that is 1.1. The different slopes can be ascribed to different fitting procedures; indeed, if we follow the ODR method, we also retrieve a super-linear slope. Regions with the largest sSFR are located in the upper envelope of this relation; in other words, cells located above the spatially resolved MS are also located above the $\log \Sigma_{\star}$ - $\log \Sigma_{\text{H}_2}$ relation. This trend, outlined also in Ellison et al. (2020b), is here as significant as the one visible in Fig. 2 for the molecular KS relation.

A correlation is also apparent between $\log \Sigma_{\star}$ and $\log \Sigma_{\text{gas}}$, that is the combination of the two behaviours seen in the left and central panel of Fig. 3. At low Σ_{\star} ($\log \Sigma_{\star} \lesssim 7$), the HI tends to dominate over H₂, and the scatter of the relation is larger, while it is slightly narrower at large Σ_{\star} . This combined behaviour results in a slope of 0.50 ± 0.14 and an intercept of -2.64 ± 0.97 , and a Spearman coefficient of 0.54. Slope and intercept of the $\log \Sigma_{\star}$ - $\log \Sigma_{\text{gas}}$ and $\log \Sigma_{\star}$ - $\log \Sigma_{\text{H}_2}$ relations are summarised in Table 2.

3.3 HI and H₂ in the Σ_{\star} - Σ_{SFR} plane

To further analyse the link between the atomic, molecular and total gas and the star formation properties of a region,

we show in Fig. 4 how $\log \Sigma_{\text{HI}}$ and $\log \Sigma_{\text{H}_2}$ vary across the $\log \Sigma_{\star}$ - $\log \Sigma_{\text{SFR}}$ plane. In the two left panels of Fig. 4 we show the $\log \Sigma_{\star}$ - $\log \Sigma_{\text{SFR}}$ plane color coded as a function of the average $\log \Sigma_{\text{HI}}$ (top) and $\log \Sigma_{\text{H}_2}$ (bottom) values in each bin. The spatially resolved MS is indicated with the black solid line. To compute the average value of $\log \Sigma_{\text{H}_2}$ we also used values below the sensitivity limit, therefore it is important to emphasise that H₂ is detected only for Σ_{H_2} above $\sim 3 M_{\odot} \text{pc}^{-2}$ which requires a Σ_{\star} higher than $10^7 M_{\odot} \text{kpc}^{-2}$. On the other hand H₂ column densities below this threshold value are hardly self-shielded and quite rare (e.g. Sternberg et al. 2014).

Interestingly, along the MS relation the average value of $\log \Sigma_{\text{HI}}$ is fairly constant and equal to about $7 M_{\odot} \text{pc}^{-2}$ which corresponds to an HI column density of about $9 \cdot 10^{20} \text{cm}^{-2}$. This indicates that for cells on the MS the radiation field is strong enough to partially dissociate H₂, and large amounts of dust rich HI gas prevent further H₂ dissociation (Sternberg et al. 2014). As expected, Σ_{H_2} increases with increasing M_{\star} , following the MGMS relation, suggesting that the gravity dominated by stars compresses and enhances the ISM volume density, thus favoring the formation of molecules. The upper envelope of the MS is populated by cells that, on average, have larger HI surface densities than counterparts located on the relation and below it. Focusing on H₂, we can see that no variations in $\log \Sigma_{\text{H}_2}$ are visible perpendicular to the MS relation, while a weak trend on increasing $\log \Sigma_{\text{H}_2}$ towards higher $\log \Sigma_{\text{SFR}}$ can be seen at fixed stellar surface density. For example, at $\log \Sigma_{\star} = 7.5$ the average value of $\log \Sigma_{\text{H}_2}$ on the MS is $0.8 M_{\odot} \text{pc}^{-2}$, and increases to $\sim 1.35 M_{\odot} \text{pc}^{-2}$ 0.8 dex above the relation. Following Eq. 2, this variation in $\log \Sigma_{\text{H}_2}$ would correspond to a difference in $\log \Sigma_{\text{SFR}}$ of ~ 0.5 dex, implying that the increase in H₂ seen at fixed stellar surface densities is not sufficient alone in setting large SFR. In the right panels of Fig. 4 we show the distance from the spatially resolved MS plotted as a function of $\log \Sigma_{\text{HI}}$ (top) and $\log \Sigma_{\text{H}_2}$ (bottom). As indicated qualitatively from Fig. 2, we observe a correlation between $\log \Sigma_{\text{HI}}$ and Δ_{MS} , for which regions located above the MS are characterized by the largest HI surface brightness, while regions below the MS correspond to cells with low $\log \Sigma_{\text{HI}}$. We do not observe any correlation between $\log \Sigma_{\text{H}_2}$ and Δ_{MS} . This is the combination of the two previous results: 1) the molecular KS relation is populated by regions on the MS, and 2) the existence of the MGMS. This suggests that the absolute quantity of molecular gas in a region (or, equivalently its surface density) is not related to the sSFR of the region itself.

3.4 Dependency of the results on metallicity

A possible source of uncertainty in this work is the dependency of the conversion factor between CO and H₂ on gas-phase metallicity (α_{CO}). Indeed, several works have shown that α_{CO} varies strongly as a function of the metallicity (e.g. Bolatto et al. 2013), and strong metallicity gradients have been found in some of the galaxies in this sample, as well as in larger samples of local star forming galaxies (Ho et al. 2014; Chiang et al. 2018; Vílchez et al. 2019), reaching a factor of 10 within the optical radius. From an integrated perspective, instead, Genzel et al. (2015) find that

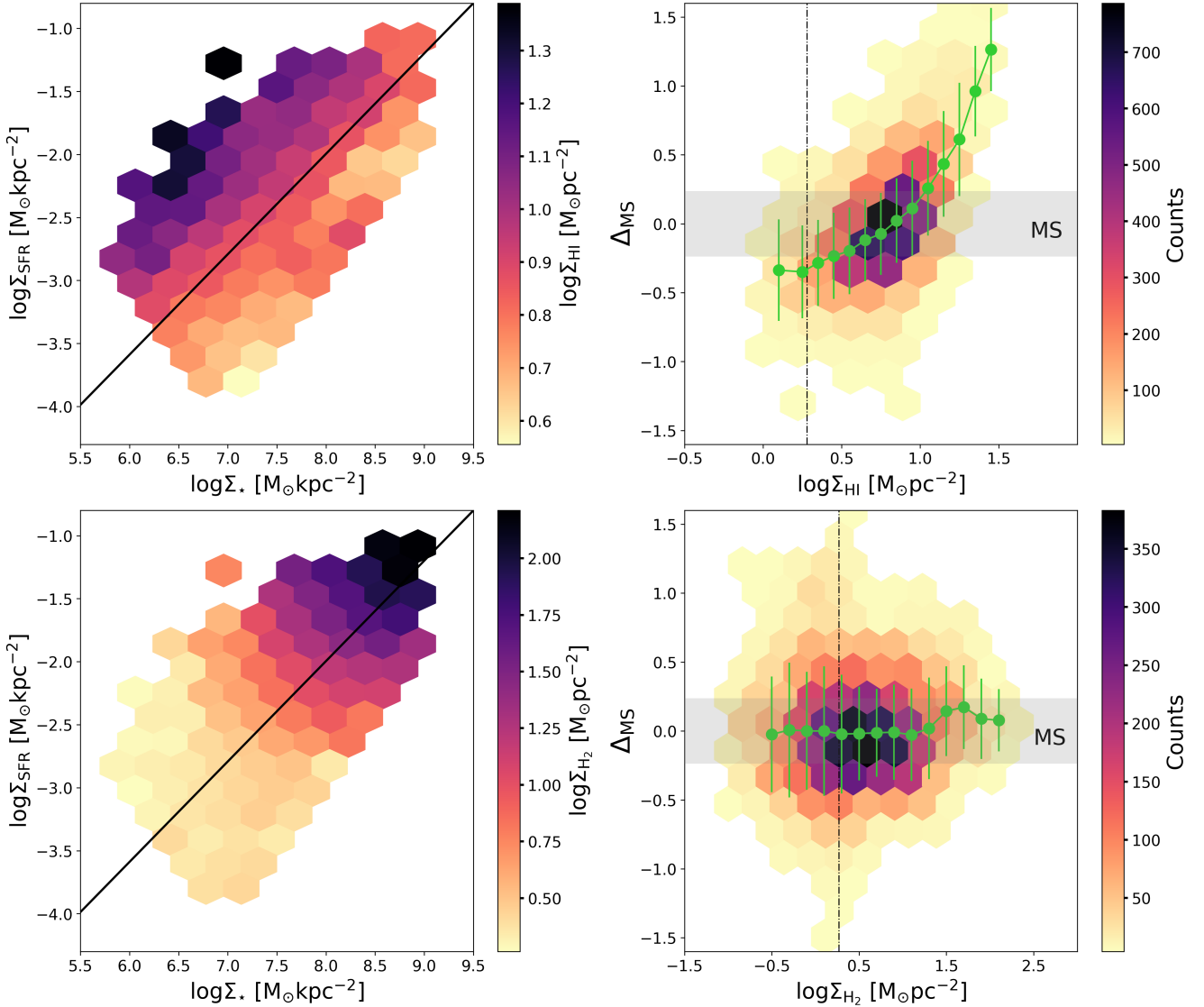


Figure 4. HI and H₂ in the $\log\Sigma_{\star} - \log\Sigma_{\text{SFR}}$ plane. *Top-left panel:* $\log\Sigma_{\star} - \log\Sigma_{\text{SFR}}$ plane color coded as a function of the average value of $\log\Sigma_{\text{HI}}$ in each bin. The black solid line marks the location of the spatially resolved MS relation. *Top-right panel:* Δ_{MS} , as a function of $\log\Sigma_{\text{HI}}$. The average values of Δ_{MS} computed in bins of $\log\Sigma_{\text{HI}}$ are shown in green. Each bin is colour coded as a function of the number of cells that it contains. *Bottom-left panel:* $\log\Sigma_{\star} - \log\Sigma_{\text{SFR}}$ plane color coded as a function of the average value of $\log\Sigma_{\text{H}_2}$ in each bin. The black solid line marks the location of the spatially resolved MS relation. *Bottom-right panel:* Δ_{MS} , as a function of $\log\Sigma_{\text{H}_2}$. The average values of Δ_{MS} computed in bins of $\log\Sigma_{\text{H}_2}$ are shown in green. Each bin is colour coded as a function of the number of cells that it contains. In the right panels, the grey shaded area marks the MS region.

α_{CO} varies little within ± 0.6 dex of the MS (thus for the large majority of the cells in this work). Nevertheless, such variations in metallicity need to be addressed properly in order to avoid biased interpretations of spatially resolved results. From the DustPedia archive, we download the table containing all the metallicity measurements available in literature (De Vis et al. 2019) and obtain in regions within R_{25} of the five galaxies in our sample. For NGC5457 there are 280 estimates of metallicity within the optical radius, while for NGC6946 only 14 are available. In particular, we make use of the metallicities computed exploiting the N2

and O3N2 calibrations of Pettini & Pagel (2004)³. In particular, N2 is defined as $\log([\text{N II}]_{6583\text{\AA}}/H_{\alpha})$ and O3N2 as $\log([\text{O III}]_{5007\text{\AA}}/H_{\beta})/([\text{N II}]_{6583\text{\AA}}/H_{\alpha})$. With the conversion relations of Kewley et al. (2004) we obtain the metallicities in the Denicoló et al. (2002) calibration. For each galaxy we then build a 1D metallicity profile by fitting the different measurements. We use the 1D metallicity profile to obtain a 2D map of the metallicity dependent α_{CO} factor exploiting the relation of Genzel et al. (2012), that is obtained by fitting the $z \sim 0$ points of Leroy et al. (2011) with $z > 1$ ones

³ We refer the reader to Casasola et al. (2020) and De Vis et al. (2019) for details of the metallicity calibration.

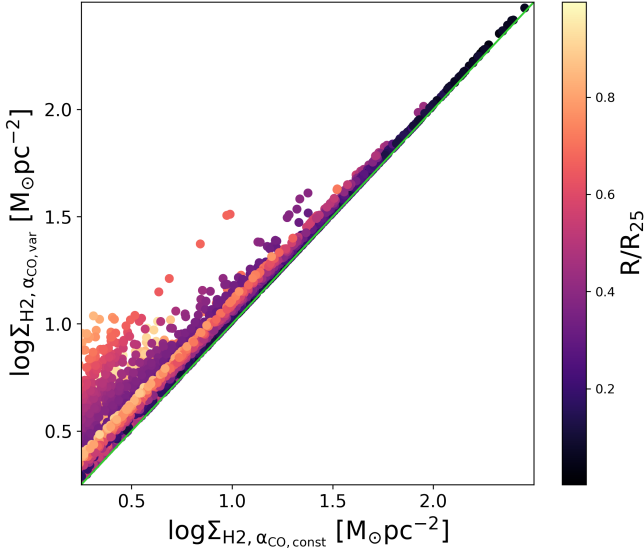


Figure 5. Comparison between the spatially resolved molecular gas mass computed with a constant α_{CO} factor and a metallicity dependent one (here for clarity we use the metallicity based on the O3N2 measurement; no significant differences are found when using the metallicity based on the N2 data). The points are colour coded as a function of their R/R_{25} value. The green solid line marks the 1 to 1 relation.

collected in [Genzel et al. \(2012\)](#):

$$\log \alpha_{\text{CO}} = -1.3 \cdot (12 + \log(O/H))_{\text{Denicolo02}} + 12 \quad (5)$$

With the 2D map of $\log \alpha_{\text{CO}}$ we then estimate Σ_{H_2} . Fig. 5 shows a comparison of the molecular gas surface density computed considering a constant α_{CO} and the metallicity dependent one (in particular, the one obtained with the O3N2 calibration, but no significant differences are found when considering the N2 one). The highest scatter corresponds to small Σ_{H_2} , located in the outskirts of the optical disc, where the metallicity is, on average, smaller than in the centre. The source characterized by the largest scatter is NGC5457, that is also the one with the strongest metallicity gradient ([Vílchez et al. 2019](#)). We note, nevertheless, that within $0.5 R_{25}$ (that is, in first approximation, the distance within which the estimate of Σ_{H_2} is above the sensitivity limit), the maximum difference between the two estimates is around 0.2 dex.

We repeat the previously shown analysis considering Σ_{H_2} estimated with the metallicity dependent α_{CO} . In Tab. 2 we report the slopes, intercepts and scatter of the various relations discussed above: $\log \Sigma_{\text{H}_2} - \log \Sigma_{\text{SFR}}$, $\log \Sigma_{\text{gas}} - \log \Sigma_{\text{SFR}}$, $\log \Sigma_{\star} - \log \Sigma_{\text{H}_2}$, and $\log \Sigma_{\star} - \log \Sigma_{\text{gas}}$. With respect to the case of constant α_{CO} , the slope of molecular KS relation slightly increases but not significantly given the errors on the estimates. The slope of the total gas KS law decreases to reach values closer to 1, but again this decrease is not significant when taking the errors into account. Similarly, the variations in slope and intercept of the $\log \Sigma_{\star} - \log \Sigma_{\text{H}_2, \text{gas}}$ relations do not vary significantly with respect to the values found in Sec. 3.2. The scatter of the four relations slightly increases. In particular, the scatter of the $\log \Sigma_{\star} - \log \Sigma_{\text{H}_2, \text{gas}}$ relations is comparable or larger than the one of the spatially resolved

MS. This is expected, as we are adding several sources of uncertainty: the conversion between different metallicity calibrations, the correlation between α_{CO} and metallicity, as well as the fact that we are averaging the metallicity to obtain a 1D profile. In first approximation, this exercise reveals that the result in this paper are robust against variations of the α_{CO} factor as a function of metallicity, that is the main and most studied dependence of α_{CO} on physical/galaxy properties (e.g., gas temperature and abundance, optical depth, cloud structure, cosmic ray density, and UV radiation field, in addition to the metallicity). This happens because the central metallicities for the galaxies in our sample are similar, and the molecular gas maps are not deep enough to reach the outermost regions where the metallicity decrease with respect to the central value.

4 DISCUSSION

4.1 The origin of the main sequence and its scatter

The spatially resolved MS of galaxies constitutes the building block of the integrated MS relation of star forming galaxies so deeply analysed in literature to understand the star formation processes and the quenching mechanisms. When analysing the molecular gas component of nearby galaxies we find tighter relations than the MS itself, and that may be at the physical origin of it: the KS law (2) and the MGMS (4). By combining Equations 2 and 4, we obtain a spatially resolved MS in the form:

$$\log \Sigma_{\text{SFR}} = 0.73 \cdot \log \Sigma_{\star} - 7.89 \quad (6)$$

that is, as expected, consistent with the spatially resolved MS relation characterising our sample ($\log \Sigma_{\text{SFR}} = 0.76 \log \Sigma_{\star} - 8.15$, see Sec. 2.1). We find that the $\Sigma_{\text{H}_2} - \Sigma_{\text{SFR}}$ relation is the tightest one of the three, with a scatter of 0.19 dex, followed by the $\Sigma_{\star} - \Sigma_{\text{H}_2}$ relation, 0.22 dex, similar to the scatter of the spatially resolved MS (0.23 dex). Contrary to [Lin et al. \(2019\)](#) we find that the scatter of the spatially resolved MS is significantly smaller than the quadratic sum of the scatters of the $\Sigma_{\star} - \Sigma_{\text{H}_2}$ and $\Sigma_{\text{H}_2} - \Sigma_{\text{SFR}}$ relations, indicating that the scatters of these relations are not independent. Indeed, regions located in the upper (lower) envelope of the molecular KS relation also populate the upper (lower) envelope of the MGMS. To further investigate the connection between the three relations (KS, MS, MGMS), we plot in the left panel of Fig. 6 how regions with an estimate of Σ_{H_2} above the sensitivity limit populate the 3D space made by $\log \Sigma_{\star}$, $\log \Sigma_{\text{SFR}}$ and $\log \Sigma_{\text{H}_2}$ (four different projections of this space are shown in Fig. A1 in Appendix A). The variables define a 3D relation, as found by [Lin et al. \(2019\)](#). This is expected, as we find no dependency of Δ_{MS} on Σ_{H_2} (see Fig. 4). On the other hand, the analysis of Σ_{HI} in the $\log \Sigma_{\star} - \log \Sigma_{\text{SFR}}$ plane revealed that the spatially resolved MS scatter seems to be connected to the presence of neutral gas. Indeed, when analysing how regions populate the 3D space formed by $\log \Sigma_{\star}$, $\log \Sigma_{\text{SFR}}$ and $\log \Sigma_{\text{HI}}$, we find that they identify a plane, as shown in the right panel of Fig. 6 (four different projections of this plane are shown in Fig. A2 in Appendix A). The equation of the plane that minimises

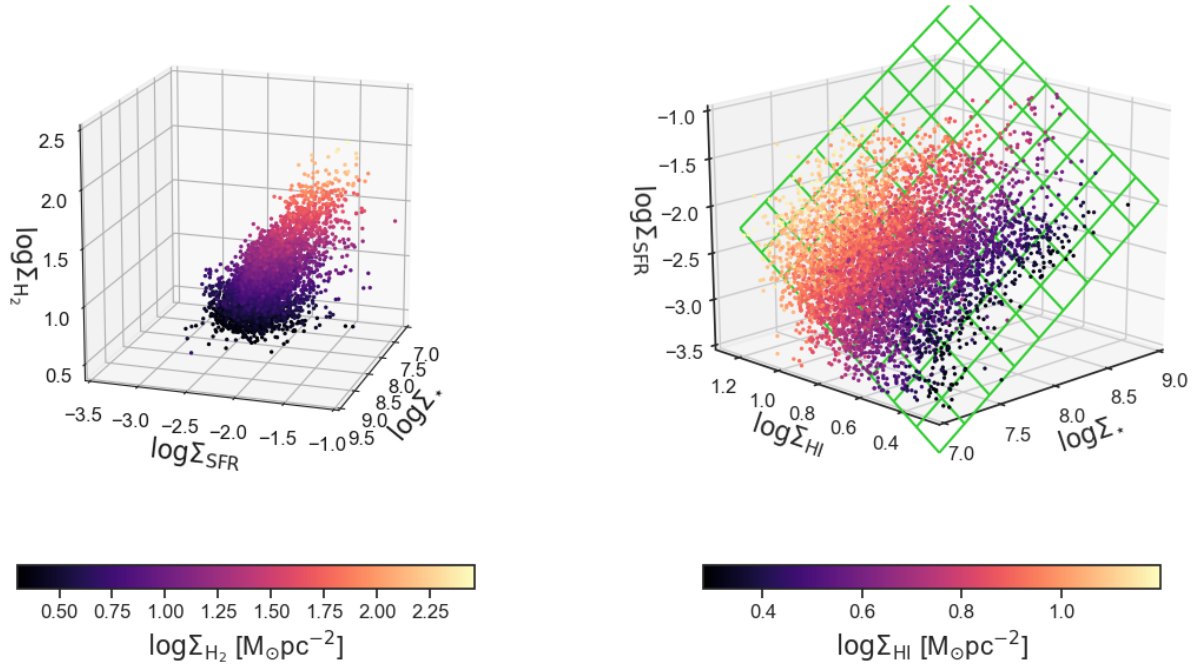


Figure 6. *Left panel:* distribution of the regions having an estimate of Σ_{H_2} above the sensitivity limit in the $\log \Sigma_{\star} - \log \Sigma_{\text{SFR}} - \log \Sigma_{\text{H}_2}$ plane. Each point is colour coded as a function of $\log \Sigma_{\text{H}_2}$. Four projections of this space at different azimuthal angles are shown in Fig. A1. *Right panel:* distribution of the regions having an estimate of Σ_{HI} above the sensitivity limit in the $\log \Sigma_{\star} - \log \Sigma_{\text{SFR}} - \log \Sigma_{\text{HI}}$ plane. Each point is colour coded as a function of $\log \Sigma_{\text{HI}}$. The best fit plane is indicated by the green grid. Four projections of this plane, described by Eq. 7, at different azimuthal angles are shown in Fig. A2.

Table 2. Slope, intercept and scatter of the following relations: molecular KS law, $\log \Sigma_{\text{gas}} - \log \Sigma_{\text{SFR}}$, MGMS and $\log \Sigma_{\star} - \log \Sigma_{\text{gas}}$. We list the best fit parameters for $\log \Sigma_{\text{H}_2}$ computed using a constant XCO factor and a metallicity dependent XCO obtained from estimates of the metallicity that use: 1) the N2 index, and 2) the O3N2 index.

| Correlation | Slope | | | Intercept | | | Scatter | | |
|---|----------------------------|-----------------|-----------------|----------------------------|------------------|------------------|----------------------------|------|------|
| | const α_{CO} | O3N2 | N2 | const α_{CO} | O3N2 | N2 | const α_{CO} | O3N2 | N2 |
| $\log \Sigma_{\text{H}_2} - \log \Sigma_{\text{SFR}}$ | 0.80 ± 0.12 | 0.83 ± 0.12 | 0.83 ± 0.11 | -2.97 ± 0.87 | -2.97 ± 0.93 | -2.94 ± 0.94 | 0.19 | 0.20 | 0.19 |
| $\log \Sigma_{\text{gas}} - \log \Sigma_{\text{SFR}}$ | 1.21 ± 0.18 | 1.24 ± 0.16 | 1.25 ± 0.18 | -3.74 ± 1.15 | -3.74 ± 1.15 | -3.73 ± 1.14 | 0.17 | 0.18 | 0.18 |
| $\log \Sigma_{\star} - \log \Sigma_{\text{H}_2}$ | 0.91 ± 0.29 | 0.84 ± 0.29 | 0.87 ± 0.27 | -6.15 ± 2.11 | -5.66 ± 2.12 | -5.93 ± 2.07 | 0.22 | 0.24 | 0.23 |
| $\log \Sigma_{\star} - \log \Sigma_{\text{gas}}$ | 0.50 ± 0.14 | 0.49 ± 0.14 | 0.49 ± 0.13 | -2.64 ± 0.97 | -2.62 ± 1.08 | -2.72 ± 1.05 | 0.24 | 0.25 | 0.25 |

the perpendicular distance of the points can be written as:

$$\log \Sigma_{\text{SFR}} = 0.97 \log \Sigma_{\star} + 1.99 \log \Sigma_{\text{HI}} - 11.11 \quad (7)$$

The relation expressed by Eq. 7 has a scatter of 0.14 dex, significantly smaller than the one of the spatially resolved MS relation. Interestingly, when the dependency of the SFR of HI surface densities is taken into account, the relation between $\log \Sigma_{\text{SFR}}$ and $\log \Sigma_{\star}$ becomes closer to linear. To better understand the origin of the relation expressed by Eq. 7, in Fig. 7 we show the $\log \Sigma_{\text{H}_2} - \log \Sigma_{\text{HI}}$ plane colour coded as a function of Δ_{MS} (left panel) and r/R_{25} (right panel). From Fig. 7 we can appreciate that regions with Σ_{HI} higher than $10 \text{ M}_{\odot} \text{ pc}^{-2}$ (that is the typical value for the HI to H2 transition, Bigiel et al. 2008; Leroy et al. 2008; Lee et al. 2012, 2014) correspond to the upper envelope of the spatially resolved MS and, on average, are preferentially located between 0.3 and 0.8 R_{25} . These regions span a wide range of $\log \Sigma_{\text{H}_2}$ values: 1) up to $\log \Sigma_{\text{H}_2} = 2 \text{ M}_{\odot} \text{ pc}^{-2}$ for $0.3 R_{25} < r < 0.6 R_{25}$, and 2) below the sensitivity limit for $r > 0.6 R_{25}$. In the first case, the stellar surface density and

average SFR are moderately high: high HI surface densities could be partially due to H_2 dissociation and are needed (together with dust) to prevent the further dissociation of the molecular gas by the intense radiation field. In the outer part of the optical disc, the SFRs are on average lower than in the inner disc, and so is the stellar surface density; nevertheless, the SFRs above the MS reach values that are comparable to SFRs on the MS in the inner part of the disc.

Most likely, once the molecular gas gives birth to new stars, it is partly disrupted by the resulting intense UV radiation from hot massive stars. To illustrate this effect, in Fig. 8 we plot the $\Sigma_{\text{H}_2}/\Sigma_{\text{HI}}$ ratio as a function of Σ_{gas} . As expected, for higher Σ_{gas} this ratio increases: H_2 becomes progressively more dominant over HI as the chemical equilibrium shifts in favor of the molecular phase with increasing gas pressure. However, the correlation is quite broad, and the origin of the spread at fixed Σ_{gas} becomes evident once the cells are color coded as a function of Δ_{MS} . Going from below to above the MS relation, $\Sigma_{\text{H}_2}/\Sigma_{\text{HI}}$ steadily decreases. We

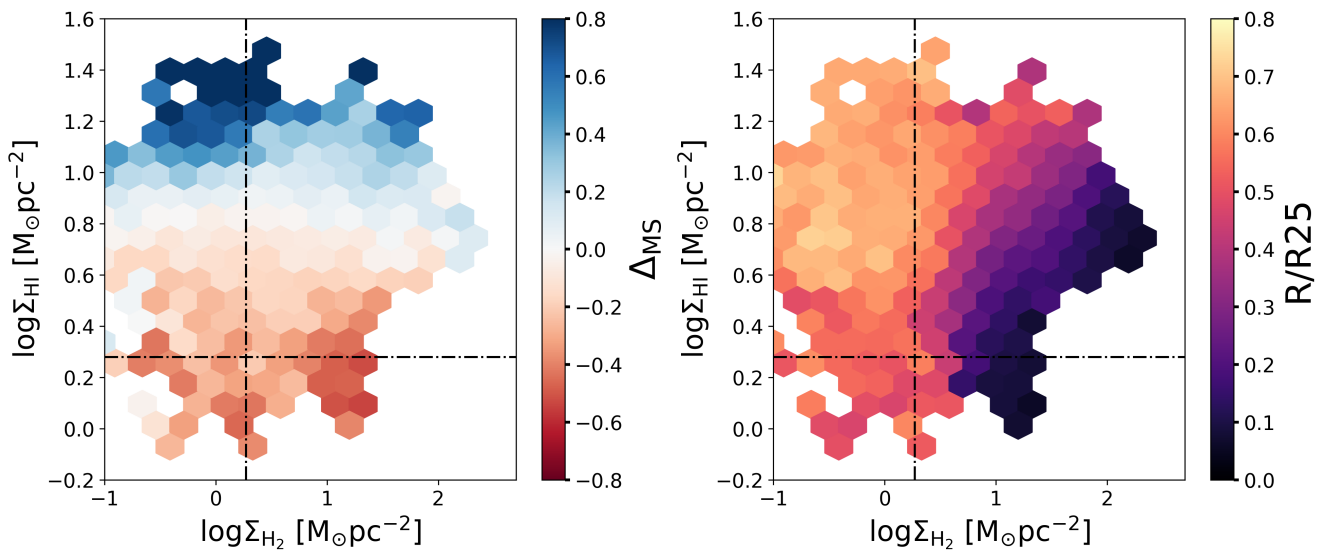


Figure 7. The $\log\Sigma_{\text{H}_2}$ - $\log\Sigma_{\text{HI}}$ plane, colour coded as a function of Δ_{MS} (left panel) and R/R_{25} (right panel). Sensitivity limits are marked with dotted-dashed lines.

interpret this trend as evidence that stellar feedback (radiative and from supernova shocks) has the effect of partially dissociating the H_2 molecules in regions of intense star formation. The sheer size of this trend is worth emphasizing, as the H_2/HI ratio drops by about a factor of 100 when going from extreme sub-MS to super-MS (starbursting) cells. Such a wide range is indeed expected by theory, for a wide variation of the intensity of the UV radiation field (cf. Figure 7 in Sternberg et al. 2014, see also Tacconi et al. 2020).

We notice that a correlation between the HI abundance and the distance from the MS has been recently reported by Wang et al. (2020) when analysing integrated galaxy properties, i.e., galaxies above the MS are more HI-rich than those below. They interpret this trend in terms of HI being an intermediate step (between the ionized and the molecular phase) in fueling star formation in galaxies, but do not consider HI as a product of molecular dissociation. Our results instead indicate that HI is also a product of star formation and its surface density is extremely sensitive to the local UV radiation field.

4.2 Star Formation Efficiency vs Gas Fraction

The data set in our hands gives us the possibility to analyse the role of SFE and f_{gas} in setting the sSFR of a region, thus deciding its location with respect to the spatially resolved MS relation. As in literature the gas fraction and SFE estimates may or may not include the contribution of neutral gas, depending on how the gas mass is measured, we define the molecular, atomic and total SFE: $\text{SFE}_{\text{mol}} = \text{SFR}/M_{\text{H}_2}$, $\text{SFE}_{\text{ato}} = \text{SFR}/M_{\text{HI}}$, $\text{SFE}_{\text{tot}} = \text{SFR}/(M_{\text{HI}}+M_{\text{H}_2})$. Similarly, we define the molecular, atomic and total gas fractions as: $f_{\text{gas,mol}} = M_{\text{H}_2}/(M_{\text{H}_2}+M_{\text{HI}}+M_{\star})$, $f_{\text{gas,ato}} = M_{\text{HI}}/(M_{\text{H}_2}+M_{\text{HI}}+M_{\star})$ and $f_{\text{gas,tot}} = (M_{\text{HI}}+M_{\text{H}_2})/(M_{\text{HI}}+M_{\text{H}_2}+M_{\star})$.

In Fig. 9 we show how the average SFE (top) and f_{gas} (bottom) vary in the $\log\Sigma_{\star}$ - $\log\Sigma_{\text{SFR}}$ plane, separating the different phases. Qualitatively, we observe

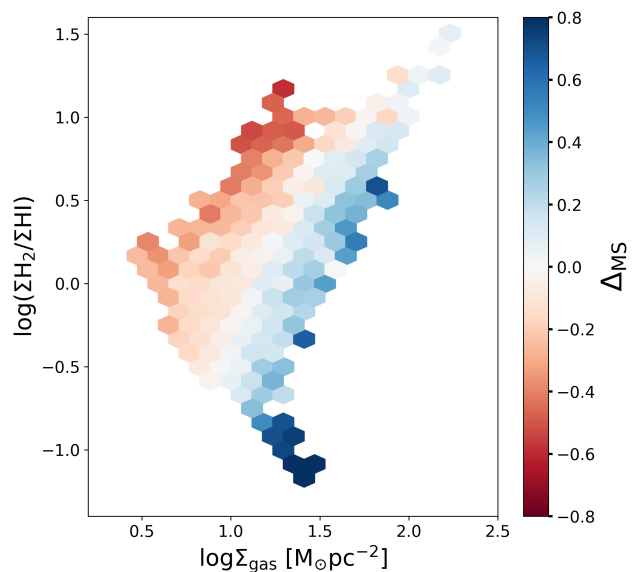


Figure 8. The $\Sigma_{\text{H}_2}/\Sigma_{\text{HI}}$ ratio as a function of Σ_{gas} . The cells have been colour coded as a function of the average Δ_{MS} .

that SFE_{mol} varies strongly above and below the MS, for $\log\Sigma_{\star} < 8M_{\odot}\text{kpc}^{-2}$, while it is almost constant at higher stellar surface densities. These trends reflect the changes in $f_{\text{gas,mol}}$, that is characterised by strong variations above/below the MS only at higher stellar surface densities, leading to a constant SFE. We notice that regions above the MS at $\log\Sigma_{\star} < 7M_{\odot}\text{kpc}^{-2}$ have very low $f_{\text{gas,mol}}$, as they are located in the outer optical disc. SFE_{ato} (central top panel) is nearly constant above/below the MS, while it steadily increases along the MS relation for increasing stellar surface densities. The atomic gas fraction is subject to two distinct trends: it decreases along the MS relation, from low to high Σ_{\star} , and tends to be higher above the MS. When considering the total gas, the variations of SFE_{tot} are less evident:

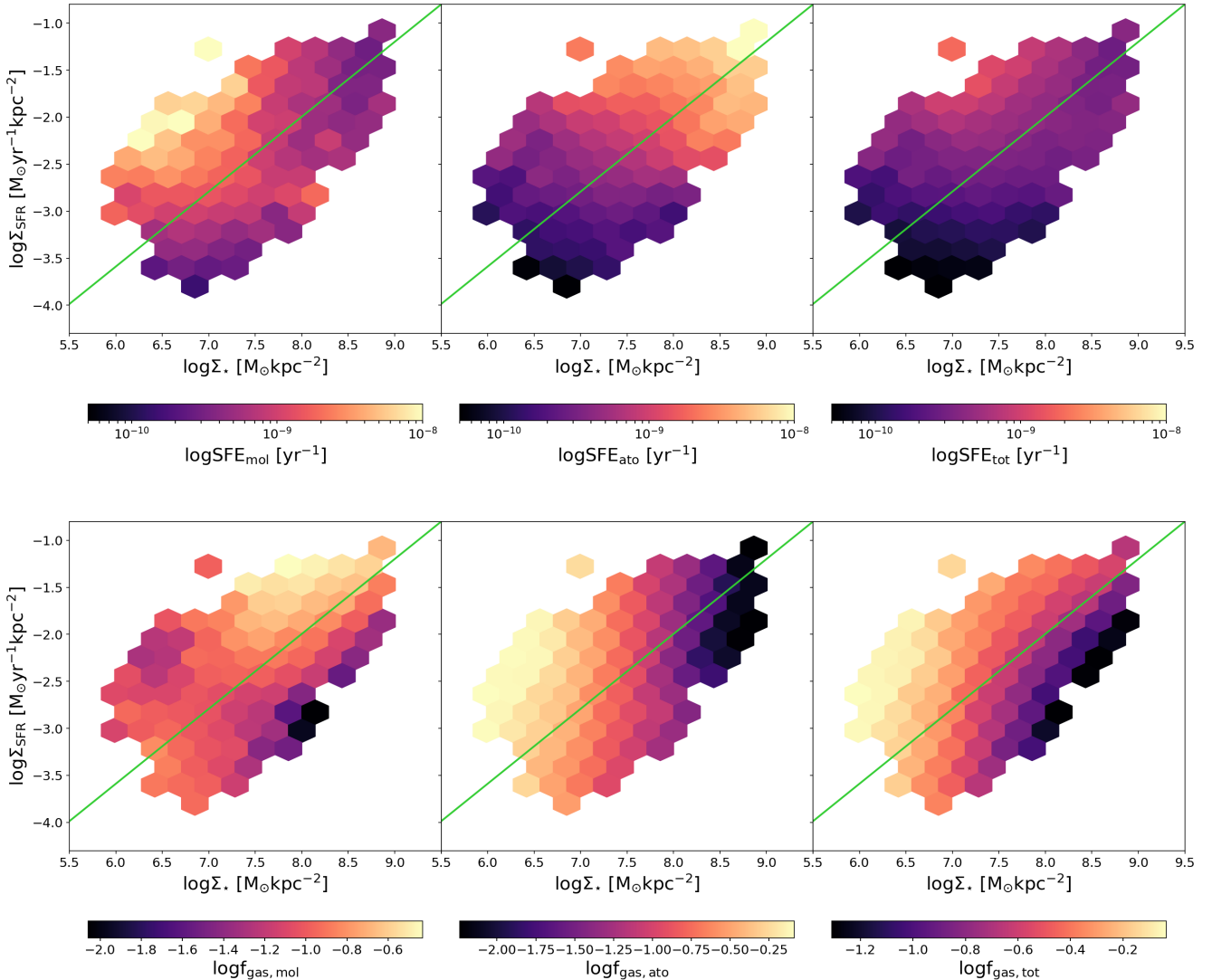


Figure 9. Molecular, atomic and total SFE and f_{gas} in the $\log \Sigma_{\star}$ - $\log \Sigma_{\text{SFR}}$ plane. The bins in the six panels are color coded as a function of: $\text{SFE}_{\text{mol}} = \text{SFR}/M_{\text{H}_2}$ in the *top left panel*, $\text{SFE}_{\text{ato}} = \text{SFR}/M_{\text{HI}}$ in the *top central panel*, $\text{SFE}_{\text{tot}} = \text{SFR}/(M_{\text{HI}}+M_{\text{H}_2})$ in the *top right panel*, $f_{\text{gas, mol}} = M_{\text{H}_2}/(M_{\text{HI}}+M_{\text{H}_2}+M_{\star})$ in the *bottom left panel*, $f_{\text{gas, ato}} = M_{\text{HI}}/(M_{\text{HI}}+M_{\text{H}_2}+M_{\star})$ in the *bottom central panel*, and $f_{\text{gas, tot}} = (M_{\text{HI}}+M_{\text{H}_2})/(M_{\text{HI}}+M_{\text{H}_2}+M_{\star})$ in the *bottom right panel*. The spatially resolved MS is indicated with the green solid line.

SFE_{tot} increases slightly at fixed stellar surface densities, less significantly in the direction perpendicular to the MS relation, and it increases along the MS for $\log \Sigma_{\star} < 7.5 M_{\odot} \text{kpc}^{-2}$, to reach an almost constant value for $\log \Sigma_{\star} > 7.5 M_{\odot} \text{kpc}^{-2}$. Finally, we observe that $f_{\text{gas, tot}}$ varies strongly when moving from the lower to the upper envelope of the MS, both perpendicular to the relation and at fixed $\log \Sigma_{\star}$. Regions with $\log \Sigma_{\star} < 7.0 M_{\odot}$, that on average correspond to $\log \Sigma_{\text{H}_2}$ below the sensitivity limit, have large gas fractions thanks to the contribution of the neutral gas.

The qualitative analysis carried on so far on Fig. 9 points to the role of both the SFE and f_{gas} in regulating the SFR of a region. From an integrated point of view, there is now convergence on the fact that an increase in SFR at fixed M_{\star} and cosmic epoch is due to a combination of increasing gas mass and decreasing depletion time (thus increasing SFE; Saintonge et al. 2011b; Saintonge et al. 2012; Leroy et al. 2013; Huang & Kauffmann 2014). In the recent years, these

studies could be carried out with larger and larger samples, using different sub-mm observations to trace gas, and exploring a wide range of cosmic epochs, $0 < z < 4.5$, with the general consensus that an almost equal increase of gas fraction and SFE can explain an increase in sSFR at fixed redshift. Scoville et al. (2017) exploited sub-mm ALMA continuum observations of 700 COSMOS galaxies at $0.3 < z < 4$ and estimated the gas mass from the dust mass. Several works in literature indicate that the dust mass is a tracer of the total gas mass (e.g. Leroy et al. 2011; Corbelli et al. 2012; Orelana et al. 2017; Casasola et al. 2020), but for $0.3 < z < 4$ the total gas is dominated by the molecular fraction (e.g. Lagos et al. 2014). Genzel et al. (2015) and Tacconi et al. (2018) combine three different estimates of molecular gas mass (from FIR SED, $\sim 1\text{mm}$ dust photometry and CO line flux) in the redshift range $0 < z < 4$ and found that an increase in sSFR at fixed stellar mass and redshift is accompanied by an almost equal increase of SFE and f_{gas} . Recently, EL-

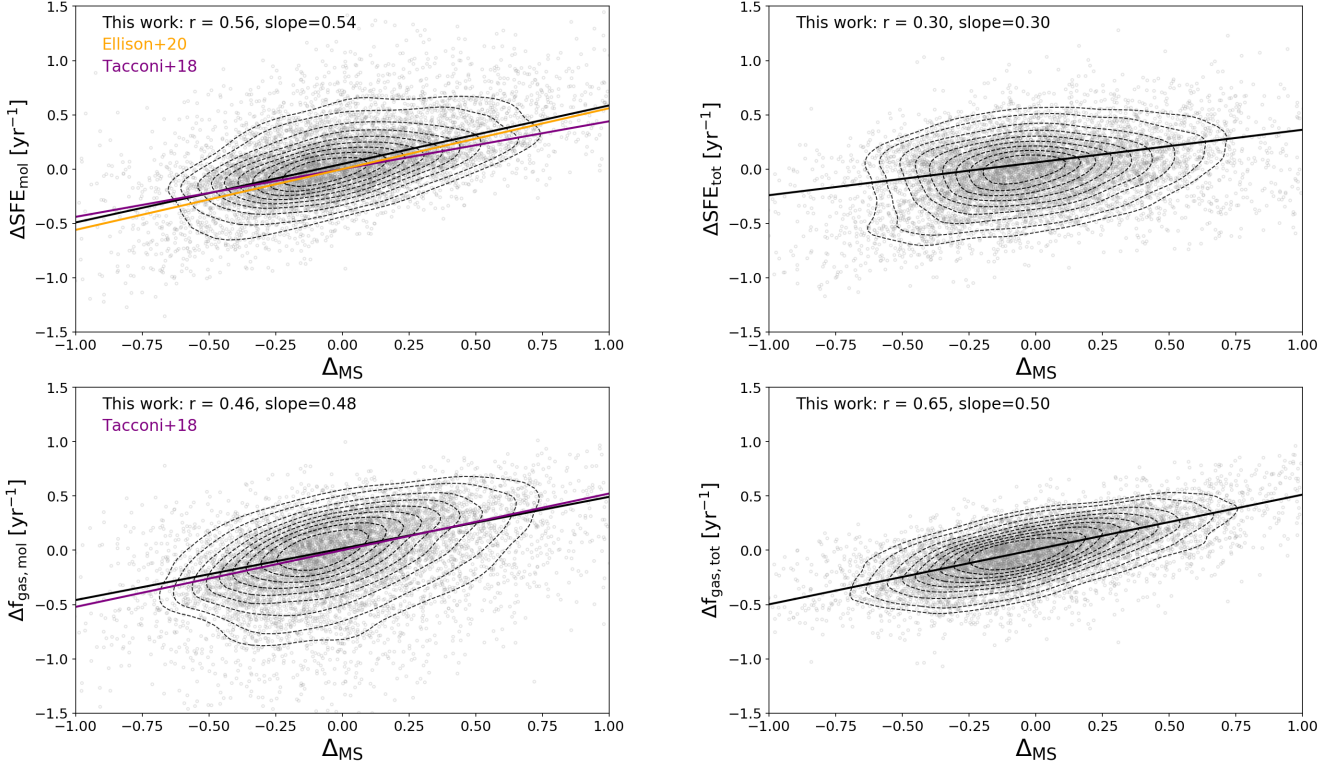


Figure 10. Distributions of regions in the $\Delta_{\text{SFE,mol}} - \Delta_{\text{MS}}$ plane (*top left panel*), in the $\Delta_{\text{SFE,tot}} - \Delta_{\text{MS}}$ plane (*top right panel*), $\Delta_{f_{\text{gas,mol}}} - \Delta_{\text{MS}}$ plane (*bottom left panel*), and $\Delta_{f_{\text{gas,tot}}} - \Delta_{\text{MS}}$ (*bottom right panel*). The best-fit relations of this work are shown as a black solid line. The best fit slope and the Pearson correlation coefficient are written each panel. In the left panels we show relations of Tacconi et al. (2018) in purple, and the one of Ellison et al. (2020) in orange.

Ellison et al. (2020b), using molecular gas observations from the ALMaQUEST survey (median redshift ~ 0.03) on kpc scales, find that variations of the SFE play a major role in setting the SFR at fixed stellar mass (and thus the scatter of the spatially resolved MS), with differences in $f_{\text{gas,mol}}$ playing a secondary role. In Fig. 10 we compare our results to the trends found in Tacconi et al. (2018) and Ellison et al. (2020b). We define Δ_{SFE} as the distance of a region from the spatially resolved KS law at fixed molecular gas mass (central panel of Fig. 2), and $\Delta_{f_{\text{gas}}}$ as the distance of a region from the spatially resolved MGMS (central panel of Fig. 3), as done in Ellison et al. (2020b). As the analysis of the connection between the scatter of these relations and Δ_{MS} in Sections 3.2 and 3.1 revealed that MS regions are located along the KS and MGMS relations, the definitions of Δ_{SFE} and $\Delta_{f_{\text{gas}}}$ given above are consistent with those of Tacconi et al. (2018), that normalise t_{depl} and f_{gas} to their MS values. The panels show the variation between molecular and total SFE and gas fraction of a region with respect to the MS values (thus Δ_{SFE} and $\Delta_{f_{\text{gas}}}$) as a function of Δ_{MS} . The top left panel shows the $\Delta_{\text{SFE,mol}} - \Delta_{\text{MS}}$ relation; the Pearson correlation coefficient is 0.56 and the best fit relation has a slope of 0.54 and a scatter of 0.18 dex, that is in excellent agreement with Tacconi et al. (2018, slope = 0.44) and Ellison et al. (2020b, slope = 0.5). We emphasise here that our work has a spatial resolution of 500 pc, thus reaching surface densities that are ~ 1 dex smaller than Ellison et al. (2020b). A similar slope (0.48) is found when analysing $\Delta_{f_{\text{gas,mol}}}$ as a function of Δ_{MS} , with a Pearson coefficient of 0.47 and a scatter of 0.23

dex. Our best fit relation is in excellent agreement with the one of Tacconi et al. (2018) (obtained from integrated quantities), that has a slope of 0.52. These results emphasise that when analysing the molecular gas phase, an increase in SFR at fixed M_{\star} and cosmic epoch is due to a combination of increasing gas mass and increasing (decreasing) SFE (t_{depl}). The situation painted by the molecular gas changes when the contribution of neutral gas is taken into account. In the left panels of Fig. 10 we show the $\Delta_{\text{SFE,tot}} - \Delta_{\text{MS}}$ (top) and the $\Delta_{f_{\text{gas,tot}}} - \Delta_{\text{MS}}$ (bottom) planes, thus considering both the neutral and molecular gas phases. Interestingly, we see that the relation between $\Delta_{\text{SFE,tot}}$ and Δ_{MS} is significantly weaker than in the molecular case, as we retrieve a Pearson coefficient of 0.30, a slope of 0.30, and a scatter of 0.28 dex. On the other hand, we observe a stronger correlation between Δ_{MS} and $\Delta_{f_{\text{gas,tot}}}$ (Spearman ranking is 0.65), with a slope of 0.50 and a scatter of 0.19 dex. These results indicate the importance of the neutral gas phase in setting the scatter of the spatially resolved MS, as it partially traces molecular gas dissociated by the radiation field.

Finally, the dataset in our hands allow us to analyse the spatial variations of SFE and f_{gas} within the 5 galaxies of the sample. The spatially resolved maps of Δ_{MS} , $\Delta_{\text{SFE,tot}}$ and $\Delta_{f_{\text{gas,tot}}}$ for every galaxy can be found in Appendix B (Figures B1 and B2). Here we emphasise that while we do observe variations within galaxies and among them of the connection between Δ_{MS} and f_{gas} or SFE, on average the galaxy by galaxy analysis confirms that the gas fraction strongly correlates with Δ_{MS} .

5 CONCLUSIONS

In this manuscript we exploit the combination of highly accurate measurements of Σ_{\star} and Σ_{SFR} at 500pc resolution of five nearby, face-on spiral galaxies obtained following the procedure presented in Paper I, with observations of neutral and molecular gas. With this powerful data set we study how the location of a region with respect to the spatially resolved Main Sequence (MS) is related to the gas in the different phases. We summarise here our main results:

- We find that $\log \Sigma_{\star}$, $\log \Sigma_{\text{SFR}}$, and $\log \Sigma_{\text{H}_2}$ define a 3D relation (left panel of Fig. 6); the three projections are the Kennicutt-Schmidt (KS) law, the MS and the molecular gas main sequence (MGMS). The KS law is the tightest relation, with a scatter of 0.19 dex, followed by the MGMS (0.22 dex) and the spatially resolved MS (0.23 dex). The existence of the MGMS at sub-kpc scales opens up the possibility to study molecular gas content from $\log \Sigma_{\text{SFR}}$ and $\log \Sigma_{\star}$ alone, that are generally easier to obtain and available for large samples;

- We study the distribution of the neutral and molecular gas in the $\log \Sigma_{\star}$ - $\log \Sigma_{\text{SFR}}$ plane (Fig. 4) and we find that the surface density of molecular gas steadily increases along the MS relation, but is almost constant perpendicular to it. The surface density of neutral gas, instead, is almost constant along the MS, and increases (decreases) in its upper (lower) envelope. On average, regions located in the upper envelope of the spatially resolved MS have $\Sigma_{\text{HI}} \geq 10 M_{\odot} \text{pc}^{-2}$, that is the typical value for the HI to H₂ transition. The three variables $\log \Sigma_{\star}$, $\log \Sigma_{\text{SFR}}$, and $\log \Sigma_{\text{HI}}$ are distributed along the plane $\log \Sigma_{\text{SFR}} = 0.97 \log \Sigma_{\star} + 1.99 \log \Sigma_{\text{HI}} - 11.11$ that has a scatter of 0.14 dex (right panel of Fig. 6);

- When moving towards high Σ_{SFR} at fixed stellar surface densities, the molecular gas fraction and molecular SFE both increase. On the other hand, when we consider the total gas, thus also the contribution of the neutral component, we observe a steep increase of the gas fraction towards high SFRs, accompanied by a weak increase of the total SFE (Fig. 10).

Our results illustrate the intricate interplay between neutral and molecular gas, as it changes radially as a function of the distance from the center of galaxies, as well as locally depending on the sSFR. We argue that molecular gas dissociation plays an important role in setting the observed trends of neutral and molecular gas surface densities around the MS relation (Fig. 8). Thus, high total gas surface densities favor the formation of molecular hydrogen clouds, which in turn promote star formation whose resulting UV radiation has the effect of dissociating the molecules, in a local baryon cycle that is a manifestation of the self-regulating nature of the star formation process. We shall return on these issues in a future paper, also expanding on their implications for our understanding of the star-formation process in high-redshift galaxies. These trends, obtained here for massive, disc-dominated spirals without a strong bar, will be analysed for galaxies with different morphologies (bulge dominated and spirals with strong bars) in another upcoming Paper.

The continuity of trends above the MS, MGMS, and KS relations suggests that starburst regions do not result from a bi-modality in the star formation process, but rather

from a steady variation of primarily the total gas fraction and partially the star formation efficiency. We speculate that this continuity could also explain the existence of high redshift starbursts, as the scatter of the spatially resolved MS is similar to the one of the integrated relation, and this last quantity is observed to be constant with redshift. It is widely believed that high redshift galaxies are dominated by H₂ over HI, because their higher gas surface density favors the molecular phase. However, this finding suggests that the higher sSFR at high redshift may actually contrast this expectation, with intense stellar feedback leading to dissociation thus reducing the H₂/HI ratio. The next generation of radio telescopes like the Square Kilometer Array (SKA), but also ongoing surveys with MeerKAT, such as MIGHTEE (Jarvis et al. 2016) and LADUMA (Blyth et al. 2016), will directly measure the HI content in distant galaxies, thus unraveling its role in the star formation processes at earlier cosmic epochs.

ACKNOWLEDGEMENTS

We thank the anonymous referee for constructive comments that improved the manuscript. LM is grateful to Sara Ellison and Bhaskar Agarwal for helpful discussion on the manuscript. LM acknowledges support from the BIRD 2018 research grant from the Università degli Studi di Padova. AE and GR are supported from the STARS@UniPD grant. GR acknowledges the support from grant PRIN MIUR 2017 - 20173ML3WW_001. GR and CM acknowledge funding from the INAF PRIN-SKA 2017 programme 1.05.01.88.04. We acknowledge funding from the INAF main stream 2018 programme "Gas-DustPedia: A definitive view of the ISM in the Local Universe". This research made use of PHOTUTILS, an Astropy package for detection and photometry of astronomical sources (Bradley et al. 2019).

DATA AVAILABILITY

This research is based on observations made with the Galaxy Evolution Explorer, obtained from the MAST data archive at the Space Telescope Science Institute, which is operated by the Association of Universities for Research in Astronomy, Inc., under NASA contract NASA 5-26555. This work made use of HERACLES, "The HERACOLine Extragalactic Survey" (Leroy et al. 2009) and THINGS, "The HI Nearby Galaxy Survey" (Walter et al. 2008). DustPedia is a collaborative focused research project supported by the European Union under the Seventh Framework Programme (2007-2013) call (proposal no. 606847). The participating institutions are: Cardiff University, UK; National Observatory of Athens, Greece; Ghent University, Belgium; Université Paris Sud, France; National Institute for Astrophysics, Italy and CEA (Paris), France. We acknowledge the usage of the HyperLeda database (<http://leda.univ-lyon1.fr>). The derived data underlying this article will be shared on reasonable request to the corresponding author.

REFERENCES

- Abdurro'uf Akiyama M., 2017, *MNRAS*, **469**, 2806
- Barrera-Ballesteros J. K., et al., 2020, *MNRAS*, **492**, 2651
- Bell E. F., Kennicutt Robert C. J., 2001, *ApJ*, **548**, 681
- Bigiel F., Leroy A., Walter F., Brinks E., de Blok W. J. G., Madore B., Thornley M. D., 2008, *AJ*, **136**, 2846
- Bigiel F., Leroy A., Walter F., Blitz L., Brinks E., de Blok W. J. G., Madore B., 2010, *AJ*, **140**, 1194
- Blitz L., Rosolowsky E., 2006, *ApJ*, **650**, 933
- Bluck A. F. L., Maiolino R., Sánchez S. F., Ellison S. L., Thorp M. D., Piotrowska J. M., Teimoorinia H., Bundy K. A., 2020, *MNRAS*, **492**, 96
- Blyth S., et al., 2016, in MeerKAT Science: On the Pathway to the SKA. p. 4
- Boissier S., Prantzos N., Boselli A., Gavazzi G., 2003, *MNRAS*, **346**, 1215
- Bolatto A. D., Wolfire M., Leroy A. K., 2013, *ARA&A*, **51**, 207
- Bolatto A. D., et al., 2017, *ApJ*, **846**, 159
- Bouché N., et al., 2010, *The Astrophysical Journal*, **718**, 1001
- Bradley L., et al., 2019, *astropy/photutils: v0.6*, doi:10.5281/zenodo.2533376, <https://doi.org/10.5281/zenodo.2533376>
- Brinchmann J., Charlot S., White S. D. M., Tremonti C., Kauffmann G., Heckman T., Brinkmann J., 2004, *Monthly Notices of the Royal Astronomical Society*, **351**, 1151
- Bundy K., et al., 2015, *The Astrophysical Journal*, **798**, 7
- Cano-Díaz M., et al., 2016, *The Astrophysical Journal Letters*, **821**, L26
- Cano-Díaz M., Ávila-Reese V., Sánchez S. F., Hernández-Toledo H. M., Rodríguez-Puebla A., Boquien M., Ibarra-Medel H., 2019, *MNRAS*, **488**, 3929
- Casasola V., Hunt L., Combes F., García-Burillo S., 2015, *A&A*, **577**, A135
- Casasola V., et al., 2017, *A&A*, **605**, A18
- Casasola V., et al., 2020, *A&A*, **633**, A100
- Chabrier G., 2003, *The Publications of the Astronomical Society of the Pacific*, **115**, 763
- Chiang I. D., Sandstrom K. M., Chasteney J., Johnson L. C., Leroy A. K., Utomo D., 2018, *ApJ*, **865**, 117
- Clark C. J. R., et al., 2018, *A&A*, **609**, A37
- Corbelli E., et al., 2012, *A&A*, **542**, A32
- Corbelli E., et al., 2017, *A&A*, **601**, A146
- Daddi E., et al., 2007, *The Astrophysical Journal*, **670**, 156
- Daddi E., et al., 2010, *ApJ*, **714**, L118
- Davies J. I., et al., 2017, *PASP*, **129**, 044102
- De Vis P., et al., 2019, *A&A*, **623**, A5
- Dekel A., et al., 2009, *Nature*, **457**, 451
- Denicoló G., Terlevich R., Terlevich E., 2002, *MNRAS*, **330**, 69
- Dey B., et al., 2019, *MNRAS*, **488**, 1926
- Elbaz D., et al., 2007, *Astronomy & Astrophysics*, **468**, 33
- Ellison S. L., Thorp M. D., Pan H.-A., Lin L., Scudder J. M., Bluck A. F. L., Sánchez S. F., Sargent M., 2020a, *MNRAS*, **492**, 6027
- Ellison S. L., et al., 2020b, *MNRAS*, **493**, L39
- Elmegreen B. G., 1993, *ApJ*, **411**, 170
- Enia A., et al., 2020, *MNRAS*,
- Ford G. P., et al., 2013, *ApJ*, **769**, 55
- Foreman-Mackey D., Hogg D. W., Lang D., Goodman J., 2013, *PASP*, **125**, 306
- Freundlich J., et al., 2013, *A&A*, **553**, A130
- Freundlich J., et al., 2019, *A&A*, **622**, A105
- Genzel R., et al., 2010, *MNRAS*, **407**, 2091
- Genzel R., et al., 2011, *ApJ*, **733**, 101
- Genzel R., et al., 2012, *ApJ*, **746**, 69
- Genzel R., et al., 2013, *ApJ*, **773**, 68
- Genzel R., et al., 2015, *ApJ*, **800**, 20
- Hall C., Courteau S., Jarrett T., Cluver M., Meurer G., Carignan C., Audcent-Ross F., 2018, *ApJ*, **865**, 154
- Ho I. T., et al., 2014, *MNRAS*, **444**, 3894
- Hopkins P. F., Kereš D., Oñorbe J., Faucher-Giguère C.-A., Quataert E., Murray N., Bullock J. S., 2014, *MNRAS*, **445**, 581
- Hsieh B. C., et al., 2017, *ApJ*, **851**, L24
- Huang M.-L., Kauffmann G., 2014, *MNRAS*, **443**, 1329
- Jarvis M., et al., 2016, in MeerKAT Science: On the Pathway to the SKA. p. 6 ([arXiv:1709.01901](https://arxiv.org/abs/1709.01901))
- Kashino D., et al., 2013, *The Astrophysical Journal Letters*, **777**, L8
- Kennicutt Robert C. J., 1998, *arXiv.org*, pp 189–232
- Kennicutt R. C., Evans N. J., 2012, *ARA&A*, **50**, 531
- Kewley L. J., Geller M. J., Jansen R. A., 2004, *AJ*, **127**, 2002
- Kruijssen J. M. D., et al., 2019, *Nature*, **569**, 519
- Krumholz M. R., McKee C. F., 2005, *ApJ*, **630**, 250
- Krumholz M. R., Dekel A., McKee C. F., 2012, *ApJ*, **745**, 69
- Kumari N., Irwin M. J., James B. L., 2020, *A&A*, **634**, A24
- Kurczynski P., et al., 2016, *ApJ*, **820**, L1
- Lagos C. d. P., Davis T. A., Lacey C. G., Zwaan M. A., Baugh C. M., Gonzalez-Perez V., Padilla N. D., 2014, *Monthly Notices of the Royal Astronomical Society*, **443**, 1002
- Lee M.-Y., et al., 2012, *ApJ*, **748**, 75
- Lee M.-Y., Stanimirović S., Wolfire M. G., Shetty R., Glover S. C. O., Molina F. Z., Klessen R. S., 2014, *ApJ*, **784**, 80
- Lee N., et al., 2017, *MNRAS*, **471**, 2124
- Leroy A. K., Walter F., Brinks E., Bigiel F., de Blok W. J. G., Madore B., Thornley M. D., 2008, *AJ*, **136**, 2782
- Leroy A. K., et al., 2009, *AJ*, **137**, 4670
- Leroy A. K., et al., 2011, *ApJ*, **737**, 12
- Leroy A. K., et al., 2013, *AJ*, **146**, 19
- Lilly S. J., Carollo C. M., Pipino A., Renzini A., Peng Y., 2013, *ApJ*, **772**, 119
- Lin L., et al., 2017, *ApJ*, **851**, 18
- Lin L., et al., 2019, *ApJ*, **884**, L33
- Makarov D., Prugniel P., Terekhova N., Courtois H., Vauglin I., 2014, *A&A*, **570**, A13
- Medling A. M., et al., 2018, *Monthly Notices of the Royal Astronomical Society*, **475**, 5194
- Mihos J. C., Harding P., Spengler C. E., Rudick C. S., Feldmeier J. J., 2013, *ApJ*, **762**, 82
- Morselli L., Popesso P., Cibinel A., Oesch P. A., Montes M., Atek H., Illingworth G. D., Holden B., 2019, *A&A*, **626**, A61
- Noeske K. G., et al., 2007, *The Astrophysical Journal*, **660**, L47
- Orellana G., et al., 2017, *A&A*, **602**, A68
- Orr M. E., et al., 2018, *MNRAS*, **478**, 3653
- Pearson W. J., et al., 2018, *A&A*, **615**, A146
- Peng Y.-j., Renzini A., 2020, *MNRAS*, **491**, L51
- Pettini M., Pagel B. E. J., 2004, *MNRAS*, **348**, L59
- Planck Collaboration et al., 2016, *A&A*, **594**, A13
- Popesso P., et al., 2019, *MNRAS*, **483**, 3213
- Rodighiero G., et al., 2011, *The Astrophysical Journal Letters*, **739**, L40
- Roychowdhury S., Huang M.-L., Kauffmann G., Wang J., Chena-galur J. N., 2015, *MNRAS*, **449**, 3700
- Saintonge A., et al., 2011a, *Monthly Notices of the Royal Astronomical Society*, **415**, 32
- Saintonge A., et al., 2011b, *MNRAS*, **415**, 61
- Saintonge A., et al., 2012, *The Astrophysical Journal*, **758**, 73
- Salim S., et al., 2007, *The Astrophysical Journal Supplement Series*, **173**, 267
- Santini P., et al., 2017, *ApJ*, **847**, 76
- Schmidt M., 1959, *ApJ*, **129**, 243
- Schreiber C., et al., 2015, *Astronomy & Astrophysics*, **575**, A74
- Schruba A., et al., 2011, *AJ*, **142**, 37
- Scoville N., et al., 2017, *ApJ*, **837**, 150
- Shetty R., Kelly B. C., Bigiel F., 2013, *MNRAS*, **430**, 288
- Shetty R., Kelly B. C., Rahman N., Bigiel F., Bolatto A. D., Clark

- P. C., Klessen R. S., Konstandin L. K., 2014a, *MNRAS*, **437**, L61
- Shetty R., Clark P. C., Klessen R. S., 2014b, *MNRAS*, **442**, 2208
- Shi Y., Helou G., Yan L., Armus L., Wu Y., Papovich C., Stierwalt S., 2011, *ApJ*, **733**, 87
- Shi Y., et al., 2018, *ApJ*, **853**, 149
- Silverman J. D., et al., 2015, *ApJ*, **812**, L23
- Silverman J. D., et al., 2018, *ApJ*, **867**, 92
- Solomon P. M., Downes D., Radford S. J. E., Barrett J. W., 1997, *ApJ*, **478**, 144
- Speagle J. S., Steinhardt C. L., Capak P. L., Silverman J. D., 2014, arXiv.org, p. 15
- Springel V., Hernquist L., 2003, *MNRAS*, **339**, 312
- Sternberg A., Le Petit F., Roueff E., Le Bourlot J., 2014, *ApJ*, **790**, 10
- Swaters R. A., van Albada T. S., van der Hulst J. M., Sancisi R., 2002, *A&A*, **390**, 829
- Tacchella S., Dekel A., Carollo C. M., Ceverino D., DeGraf C., Lapiner S., Mand elker N., Primack Joel R., 2016, *MNRAS*, **457**, 2790
- Tacconi L. J., et al., 2010, *Nature*, **463**, 781
- Tacconi L. J., et al., 2013, *ApJ*, **768**, 74
- Tacconi L. J., et al., 2018, *ApJ*, **853**, 179
- Tacconi L. J., Genzel R., Sternberg A., 2020, arXiv e-prints, p. arXiv:2003.06245
- Tan J. C., 2000, *ApJ*, **536**, 173
- Vílchez J. M., Relaño M., Kennicutt R., De Looze I., Mollá M., Galametz M., 2019, *MNRAS*, **483**, 4968
- Vulcani B., et al., 2019, *MNRAS*, **488**, 1597
- Walter F., Brinks E., de Blok W. J. G., Bigiel F., Kennicutt Robert C. J., Thornley M. D., Leroy A., 2008, *AJ*, **136**, 2563
- Wang J., et al., 2013, *MNRAS*, **433**, 270
- Wang J., Catinella B., Saintonge A., Pan Z., Serra P., Shao L., 2020, arXiv e-prints, p. arXiv:2001.01970
- Whitaker K. E., van Dokkum P. G., Brammer G., Franx M., 2012, *The Astrophysical Journal Letters*, **754**, L29
- Wyder T. K., et al., 2009, *ApJ*, **696**, 1834
- da Cunha E., Charlot S., Elbaz D., 2008, *MNRAS*, **388**, 1595
- de los Reyes M. A. C., Kennicutt Robert C. J., 2019, *ApJ*, **872**, 16

APPENDIX A: THE $\log \Sigma_{\star} - \log \Sigma_{\text{SFR}} - \log \Sigma_{\text{H}_2, \text{HI}}$ 3D RELATION

As shown in Fig. 6, the three quantities $\log \Sigma_{\star}$, $\log \Sigma_{\text{SFR}}$ and $\log \Sigma_{\text{H}_2}$ define a 3D relation. To better visualise this relation, in Fig. A1 we show four different projections of it, corresponding to azimuthal angles of 0° , 60° , 120° and 180° . We stress here that we are plotting only the regions that have an estimate of Σ_{H_2} above the sensitivity limit. In Fig. A2 we show, instead, the $\log \Sigma_{\star}$, $\log \Sigma_{\text{SFR}}$ and $\log \Sigma_{\text{HI}}$ 3D plane at four different azimuthal angles, with the aim of better visualise the positioning of the cells along the 3D plane marked in green. We plot in Fig. A2 only the regions that have an estimate of Σ_{HI} above the sensitivity limit.

APPENDIX B: Δ_{MS} , SFE AND GAS CONTENT WITHIN GALAXIES

In this Section, we discuss the distributions of Δ_{MS} , $\Delta_{\text{f}_{\text{gas}, \text{tot}}}$ and $\Delta_{\text{SFE}, \text{tot}}$ within the five galaxies in our sample, shown in Figures B1 and B2. We recall here that $\Delta_{\text{SFE}, \text{tot}}$ and $\Delta_{\text{f}_{\text{gas}, \text{tot}}}$ are computed as the distance of the region from the global total gas - SFR relation (right panel of Fig. 2) and from the

global total gas-mass relation (right panel of Fig. 3), and are thus a measure of the SFE and gas content with respect to the value on the best fitted relation at a given gas or stellar surface density (e.g. regions with $\Delta_{\text{f}_{\text{gas}, \text{tot}}} > 0$ have higher gas content than the average).

It is clear that the $\Delta_{\text{SFE}, \text{tot}}$ and the $\Delta_{\text{f}_{\text{gas}, \text{tot}}}$ in the inner regions will be anti correlated because the regions where the bulk of molecular hydrogen is are not spatially coincident with the regions where the FUV star formation tracer peaks. This is due to the time delay between the formation of molecular clouds and the exposed phase of star formation (Corbelli et al. 2017). In the inner regions of spiral galaxies the spiral pattern rotates slower than the stars and hence molecular clouds form out of compressed gas along the inner part of the arm. These are the regions with higher gas fraction than the average. The young stars become visible after dispersing the original gas and, moving faster than the arm, they appear shifted with respect to the newly formed molecular complexes. These are regions with low gas content but numerous visible young stars, hence appear with a star formation efficiency above the average. For the outer regions, at or beyond corotation, the situation should reverse with respect to the arm but the anticorrelation between $\Delta_{\text{SFE}, \text{tot}}$ and the $\Delta_{\text{f}_{\text{gas}, \text{tot}}}$ should still hold. Here the low surface density of molecules and the presence of external perturbations make the study more challenging: tidal perturbations, gas stripping and infall have a strong impact and this reflects on Δ_{MS} which can vary substantially from one region to the next, being star forming regions more coarsely spaced in the outer disks. Below we describe a few selected regions in each galaxy more in detail:

- The central region of NGC0628, i.e. the bulge, is located below the MS and has low gas content, while $\Delta_{\text{SFE}, \text{tot}}$ varies of ± 0.3 dex around zero. Regions located in the upper envelope of the MS relation are located mostly along the spiral arms. We observe regions where $\Delta_{\text{MS}} \sim 0$ (A, B and C) or $\Delta_{\text{MS}} \sim 1$ (D), or $\Delta_{\text{MS}} \sim -1$ (E), all with low gas fractions and high or average SFE.

- NGC3184 also has a central region characterised by mostly negative Δ_{MS} and $\Delta_{\text{f}_{\text{gas}, \text{tot}}}$, while $\Delta_{\text{SFE}, \text{tot}}$ is, for the majority of cells, positive. In the spiral arms, we observe regions where the SFR is significantly higher than the MS value (B and C) that correspond to gas fractions above the average, and varying SFE. We identify three blobs (A, D & E) with negative $\Delta_{\text{f}_{\text{gas}, \text{tot}}}$ and Δ_{MS} varying slightly around the MS value (as in A & E) or $\Delta_{\text{MS}} < 0$ (as in D).

- NGC5194 is characterised by a central region that has SFR values mostly above the MS. Positive values of Δ_{MS} are located mainly along the spiral arms, that are also well traced by an excess of total gas compared to the average. The regions A, B, C and D are all above the MS relation, but they show different properties: while the majority of pixels within C and D are have $\Delta_{\text{f}_{\text{gas}, \text{tot}}} > 0$ and $\Delta_{\text{SFE}, \text{tot}} \sim 0$, A and B show clumps of $\Delta_{\text{SFE}, \text{tot}}$ well above 0 and $\Delta_{\text{f}_{\text{gas}, \text{tot}}}$ varying between negative and positive values.

- NGC5457 is characterised by two strong spiral arms with several blobs that have a SFR higher than the MS value (regions A, B, C, D, E). Within these regions we observe gas fractions that are almost always higher than the MS values, while $\Delta_{\text{SFE}, \text{tot}}$ varies more strongly between positive and negative values. Region F, for which the majority of

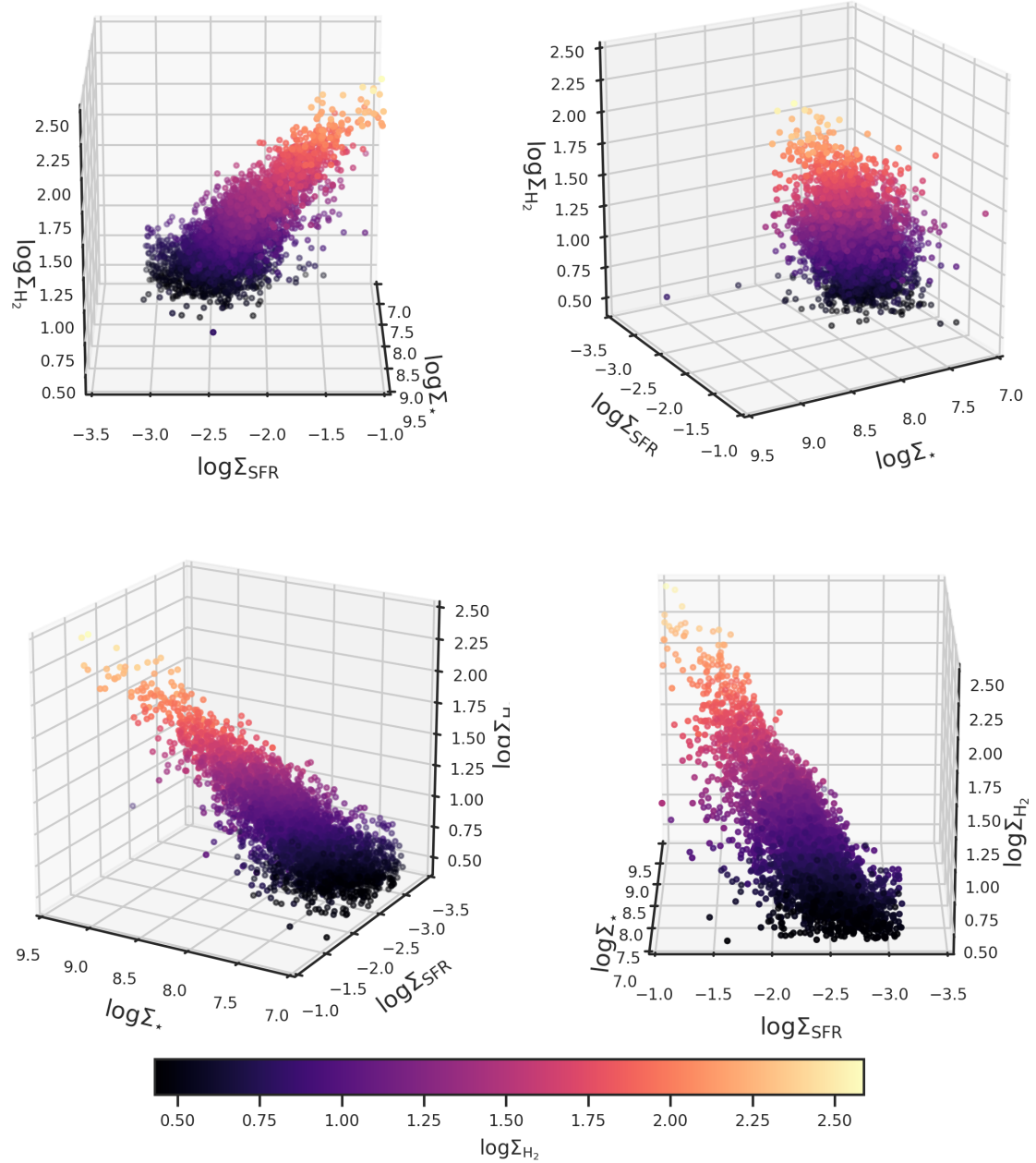


Figure A1. Distribution of the regions with an estimate of $\log \Sigma_{\text{H}_2}$ above the sensitivity limit in the $\log \Sigma_*$ - $\log \Sigma_{\text{SFR}}$ - $\log \Sigma_{\text{H}_2}$ 3D space. For different projections of the plane are shown, corresponding to different azimuthal angles: 0° (top left), 60° (top right), 120° (bottom left) and 180° (bottom right). The points are colour coded as a function of $\log \Sigma_{\text{HI}}$.

cells are well below the MS relation, has $\Delta_{\text{SFE,tot}} \sim 1$, but $\Delta_{f_{\text{gas,tot}}} \sim -1$.

- NGC6946 has a central region characterised by SFR higher than MS values, high gas content and SFE lower than the average (region B). Regions A, C and D are also characterised by values of Δ_{MS} close to 1, but different SFE. While regions A and D have close to normal gas content and SFE above the average, the more central regions B and C have a high gas content but a low SFE.

In general we conclude that in the innermost and outer

regions the decrease or enhancement of the local gas content follows closely that of the star formation rate along the MS. For the innermost region and the spiral arms the enhancement or decrease of the SFE is opposite to that of the local gas content. But there are exceptions to this behaviour. Given the possible temporal and spatial lag between molecular and FUV peaks (Krujissen et al. 2019) the relation between $\Delta_{\text{SFE,tot}}$ and Δ_{MS} for individual galaxies is more complex and requires dedicated analysis.

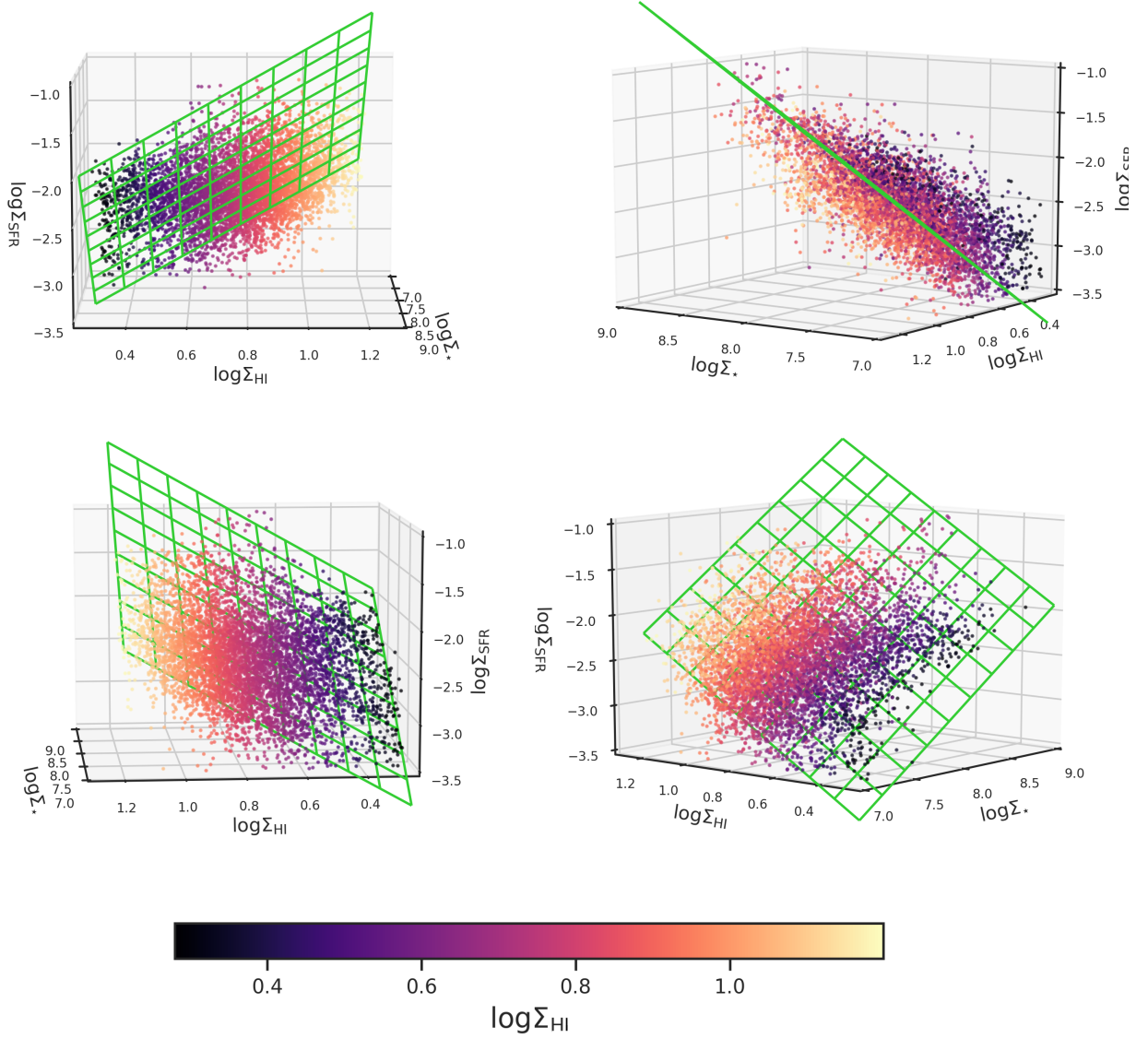


Figure A2. Distribution of the regions with an estimate of $\log \Sigma_{\text{HI}}$ above the sensitivity limit in the $\log \Sigma_{\star}$ - $\log \Sigma_{\text{SFR}}$ - $\log \Sigma_{\text{HI}}$ 3D space. For different projections of the plane are shown, corresponding to different azimuthal angles: 0° (top left), 125° (top right), 175° (bottom left) and 220° (bottom right). The point are colour coded as a function of $\log \Sigma_{\text{H}_2}$.

This paper has been typeset from a $\text{\TeX}/\text{\LaTeX}$ file prepared by the author.

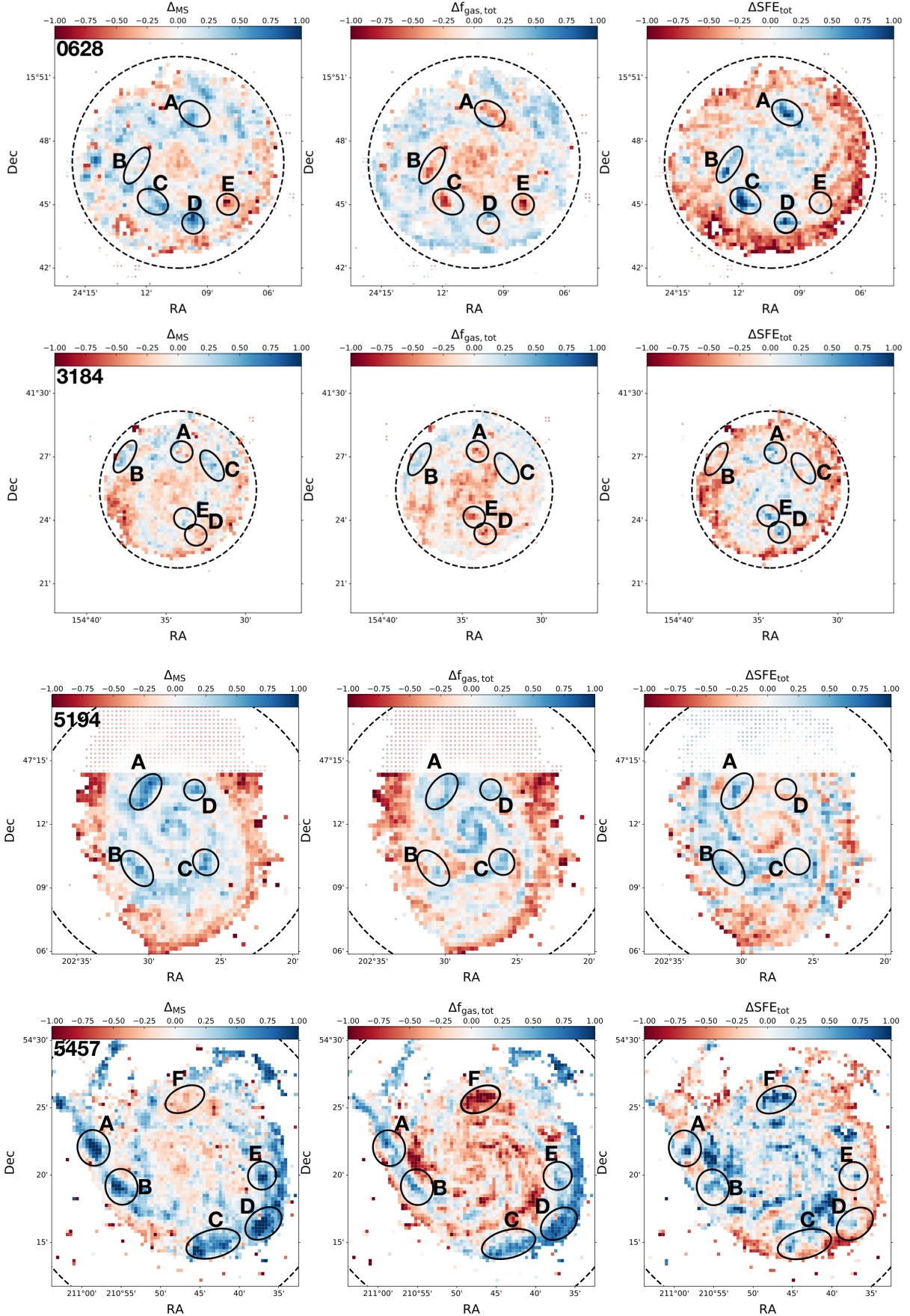


Figure B1. Δ_{MS} (left), $\Delta f_{gas,tot}$ (centre) and ΔSFE_{tot} (right) maps of (from top to bottom) NGC0628, NGC3184, NGC5194, and NGC5457. The high-galaxy region (HGR) are discussed more in detail in the text.

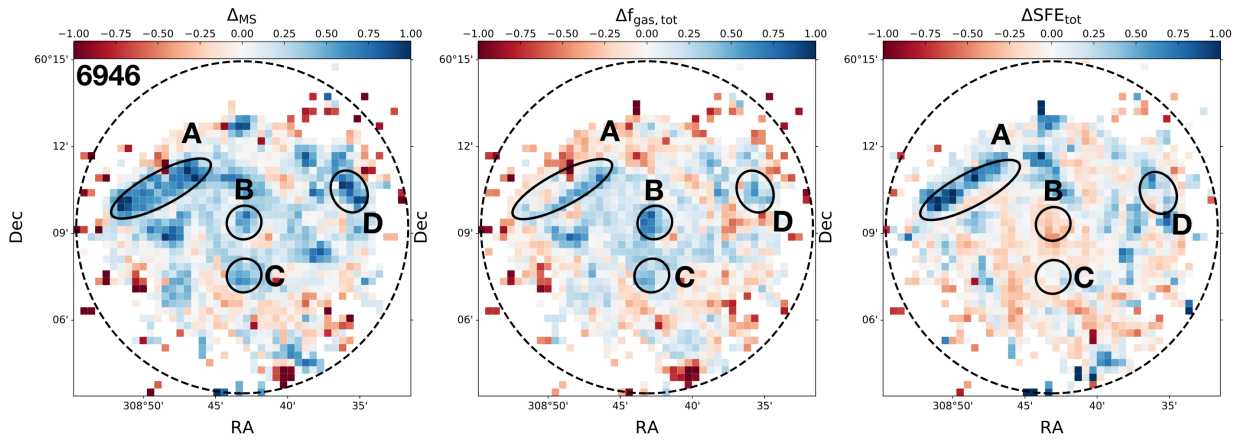


Figure B2. Δ_{MS} (left), $\Delta f_{gas,tot}$ (centre) and ΔSFE_{tot} (right) maps of NGC6946. The highlighted regions are discussed more in detail in the text.